

Structure of Silicon-Based Thin Film Solar Cell Materials

**Annual Technical Progress Report
1 April 2002–31 August 2003**

D.L. Williamson
*Colorado School of Mines
Golden, Colorado*



NREL

National Renewable Energy Laboratory

1617 Cole Boulevard
Golden, Colorado 80401-3393

NREL is a U.S. Department of Energy Laboratory
Operated by Midwest Research Institute • Battelle

Contract No. DE-AC36-99-GO10337

Structure of Silicon-Based Thin Film Solar Cell Materials

**Annual Technical Progress Report
1 April 2002–31 August 2003**

D.L. Williamson
*Colorado School of Mines
Golden, Colorado*

NREL Technical Monitor: B. von Roedern

Prepared under Subcontract No. XDJ-2-30630-27



NREL

National Renewable Energy Laboratory

1617 Cole Boulevard
Golden, Colorado 80401-3393

NREL is a U.S. Department of Energy Laboratory
Operated by Midwest Research Institute • Battelle

Contract No. DE-AC36-99-GO10337

This publication was reproduced from the best available copy submitted by the subcontractor and received no editorial review at NREL.

NOTICE

This report was prepared as an account of work sponsored by an agency of the United States government. Neither the United States government nor any agency thereof, nor any of their employees, makes any warranty, express or implied, or assumes any legal liability or responsibility for the accuracy, completeness, or usefulness of any information, apparatus, product, or process disclosed, or represents that its use would not infringe privately owned rights. Reference herein to any specific commercial product, process, or service by trade name, trademark, manufacturer, or otherwise does not necessarily constitute or imply its endorsement, recommendation, or favoring by the United States government or any agency thereof. The views and opinions of authors expressed herein do not necessarily state or reflect those of the United States government or any agency thereof.

Available electronically at <http://www.osti.gov/bridge>

Available for a processing fee to U.S. Department of Energy and its contractors, in paper, from:

U.S. Department of Energy
Office of Scientific and Technical Information
P.O. Box 62
Oak Ridge, TN 37831-0062
phone: 865.576.8401
fax: 865.576.5728
email: reports@adonis.osti.gov

Available for sale to the public, in paper, from:

U.S. Department of Commerce
National Technical Information Service
5285 Port Royal Road
Springfield, VA 22161
phone: 800.553.6847
fax: 703.605.6900
email: orders@ntis.fedworld.gov
online ordering: <http://www.ntis.gov/ordering.htm>



Printed on paper containing at least 50% wastepaper, including 20% postconsumer waste

1. EXECUTIVE SUMMARY

1.1 PREFACE

This report presents results of Phase I research performed from April 1, 2002 to August 31, 2003 under a cost-reimbursable subcontract from the National Renewable Energy Laboratory (NREL, a national laboratory of the U.S. Department of Energy operated by Midwest Research Institute) to the Colorado School of Mines (subcontract number XDJ-2-30630-27 to the prime contract DE-AC36-99GO10337). The research was carried out under the direction of Don L. Williamson, Research Professor of Physics. Materials characterization, including small-angle x-ray scattering and x-ray diffraction, was carried out in the Physics Department of the Colorado School of Mines (CSM). Transmission electron microscopy (TEM) was carried out by the co-P.I., Eli Sutter, with facilities on the CSM campus. A second co-P.I., David Marr, contributed to the analysis and publication of results from small-angle neutron scattering experiments. The materials for analyses were supplied by NREL-supported device-making groups as well as by other groups with relevant expertise. CSM undergraduate students assisted with TEM sample preparation.

1.2 OBJECTIVES/APPROACH

The purpose of this research, as part of the R&D Partner Category, is to achieve a better understanding in order to improve materials used as the intrinsic layers of amorphous and microcrystalline silicon-based solar cells. Fundamental structural properties will be investigated on atomic and nano-scales. A powerful combination of techniques will be used: analytical high-resolution transmission electron microscopy (HRTEM), including special associated spectroscopic methods, small-angle scattering techniques (SAXS, ASAXS, SANS) and conventional wide-angle x-ray diffraction (XRD). The subcontractor will actively participate in National R&D Team activities.

1.3 CONCLUSIONS

1.3.4 Transmission Electron Microscopy Experiments (Task 1)

TEM Study of a-Si:H and a-Si:D Solar Cell Materials

Cross-sectional HRTEM (XTEM) has been performed on three films previously studied by SANS. A matched pair of a-Si:H and a-Si:D films was prepared by high H/D dilution PECVD at USSC. The a-Si:H film is homogeneous with no evidence of microvoids or other mass density

fluctuations, while the a-Si:D film is highly heterogeneous with clear formation of microcrystals and microvoids/low-density D-rich regions. Both films show growth of an epitaxial Si layer at the c-Si/a-Si interface. The microvoids/D-rich regions have both spherical-like and elongated shapes. The latter are unusual in that they are elongated in-plane rather than along the growth direction as previously observed by SAXS for many films. This shape is attributed to a high in-plane compressive stress. In addition, many of the microcrystals are observed to be needle-like in shape, along the growth direction. Results for both the a-Si:H and a-Si:D films are consistent with the SANS results but provide more details of the microstructure.

The third a-Si:H film examined by XTEM was made by high-rate (10 nm/s) HWCVD at NREL. Clear heterogeneity in the form of microvoids are observed throughout the thickness of the film. Both spherical like and slightly elongated shapes are found. In this case the elongations are typically along the growth direction, consistent with previous SAXS/SANS analyses of this ultra-high-rate material. The sizes of the microvoids are around 5 nm, consistent with the SANS results on the same film.

TEM Study of a-SiGe:H Alloys

Two different a-SiGe:H films have been examined by XTEM. Both were prepared for earlier SANS studies. The NREL HWCVD alloy with 15 at.% Ge is highly heterogeneous with elongated features along the growth direction that may be microvoids, low density H-rich regions, or Ge composition fluctuations. The structural inhomogeneity features undergo a change from almost spherical at the film/substrate interface to highly elongated with increasing thickness of film. The lateral sizes of the features are 1-2 nm, consistent with SAXS/SANS interpretation. The USSC PECVD alloy with 40 at.% Ge is more homogeneous, but elongated, low-density features are clearly present. There is a correlation of the surface-emergence of these features and the surface roughness. To our knowledge, these are the first TEM observations of highly elongated, low-density features in device-quality a-SiGe:H alloys.

TEM Study of Nano- and Microcrystalline-Si Solar Cells and Materials

Five different nano- and microcrystalline Si devices and films have been investigated by XTEM. Two solar cells made by MVSsystems were studied to search for differences in microstructure due to two types of TCO layers: Asahi TCO on glass and AIST textured ZnO on

glass. The high surface roughness of the Asahi TCO leads to $\mu\text{c-Si}$ grain collisional behavior as the grains grow away from the TCO surface. Although considerable thickness variation is seen in the textured ZnO layer, its more gradual changes in lateral steepness reduces the grain collisional behavior. Microvoid formation seems to be correlated with grain collision regions. The reduced collisional behavior for the textured ZnO-based solar cell correlates with the observed improvement in device efficiency ($\sim 8.0\%$ vs. 6.8%).

One film made by HWCVD on Al-coated glass at IEC was found to consist of relatively large micrometer-sized grains, probably caused by metal-induced interdiffusion and recrystallization. This technique may prove useful for grain-size enhancement but the likely presence of Al-doping of the $\mu\text{c-Si}$ may be problematical for i-layers in cells.

Two $\mu\text{c-Si:H}$ films made in the Real-Time-Spectroscopic-Ellipsometry (RTSE) chamber at NREL have been studied to search for features needed for modeling the SE data. Delamination problems complicated the sample preparation and the imaging of the film/substrate interface. Both films were similar. The Si growth starts as amorphous and around 200 nm nanocrystalline (nc), cone-like growth begins. Immediately, with the onset of nc-Si cone-like growth, microvoids are seen to form where two cones intersect. This onset of enhanced non-uniformity due to microvoids correlates with the strong enhancement in SAXS for all nc/ $\mu\text{c-Si}$ materials studied to date.

1.3.1 Small-Angle Scattering Experiments (Task 2)

SANS Quantitative Interpretation

The heterogeneity of a-Si:H, a-Si:HD and a-Si:D films has been probed on the nano-scale by small-angle neutron scattering (SANS). Films were deposited by two techniques, plasma-enhanced chemical-vapor deposition (PECVD) and hot-wire chemical-vapor deposition (HWCVD) using conditions that yield high-quality films and devices. Thin films about 2- μm -thick grown by PECVD show both large (> 20 nm) and small (< 8 nm) heterogeneous features. The absolute SANS intensities, however, are small and place stringent upper limits on the degree of H heterogeneity present. Based on careful modeling, these results do not support a recently proposed two-domain, amorphous/paracrystalline model. The presence of a small amount of microcrystallinity in one a-Si:D film yields much stronger SANS intensities, consistent with D accumulation in voids or grain boundary regions. A clear correlation of the larger scattering features with film surface roughness is found.

The best quality HWCVD films show significant H non-uniformity, as well as a small fraction of microvoids. Two- or three-phase models are used to interpret the data quantitatively. Samples grown with higher deposition rates or lower substrate temperatures have much larger void fractions. The size scale of the heterogeneity spans a range from 2 nm to more than 50 nm, with the larger features assigned to surface roughness.

SAXS Study of BP-Solar a-Si:H Deposition Rate Series

A series of a-Si:H films was prepared with increasing deposition rate from 0.1 nm/s up to 1.0 nm/s by BP-Solar and characterized by several team members. The same material was incorporated into solar cells for comparison of device performance with the material properties. A strong correlation is found between increases in SAXS-determined microvoid density and degradation in device performance with increasing deposition rate. We also analyzed the IR data from NREL and demonstrated a similar strong correlation in IR microstructure factor with cell degradation.

SAXS Study of HWCVD a-SiGe:H Alloys

Systematic series of a-Si_{1-x}Ge_x:H alloys were prepared at NREL by HWCVD. Three primary variables were investigated: (a) Ge content-x, (b) filament temperature, and (c) substrate temperature. SAXS results demonstrate: (a) there is a strong increase in heterogeneity beginning above $x = 0.2$, consistent with our prior work on PECVD alloys; (b) for high x (Tauc gap ~ 1.3 eV) there is a significant reduction in heterogeneity as the filament temperature is lowered; (c) again for high x there is an optimum substrate temperature (at fixed filament temperature) that yields a minimum in heterogeneity. All three results correlate strongly with the photoconductivity of the films. These optimized materials show better properties (at high x) than previous alloys made by PECVD.

SAXS Study of HWCVD a-Si:H Deposited at High Rate with H Dilution

NREL is attempting to improve the microstructure of the ultra-high deposition rate HWCVD material by using hydrogen dilution. Three samples have been prepared for SAXS at rates near 10 nm/s. The results when compared to the earlier results for non-hydrogen-diluted films indicate that the microstructure has not been improved significantly. The sizes of the scattering

features are also similar to those from the earlier films. The lack of improvement in microstructure is correlated with a lack of improvement in the photoresponse found to date with such hydrogen-diluted material.

SAXS Study of USSC Microcrystalline Solar Cell Materials

Three microcrystalline-Si:H films were provided by USSC. They were fabricated with three different techniques: RF-, VHF-, and microwave-PECVD. These produce increasing deposition rates. Both SAXS and flotation density measurements were completed. Tilting SAXS was done to look for oriented microstructure. The intensities are high from all three and show slightly different shapes, indicating different size distributions of scattering objects. All three have some oriented microstructure but it is more significant in the RF and VHF samples. SAXS intensities increase systematically with deposition rate implying more heterogeneity with increasing rate. Flotation densities are quite high (similar to void-free a-Si:H), probably due to lower bonded H contents in these microcrystalline films.

SAXS Study of KAIST Photo-CVD a-Si:H Films

At the request of a group in the Department of Electrical Engineering and Computer Science of the Korea Advanced Institute of Science and Technology (KAIST), we have analyzed a series of a-Si:H films prepared by photo-CVD. The focus was on the transition from protocrystalline to the mixed amorphous/microcrystalline regime and hydrogen dilution was the variable in the series. They had postulated that there was an increase in microvoids in the protocrystalline regime prior to microcrystallite formation. However, the SAXS intensities remained extremely low until microcrystallites were detected by XRD, after which the intensities became strong. The films in the protocrystalline regime are very homogeneous and similar in structural quality with the best films we have analyzed that were grown by PECVD and HWCVD. Thus, their postulate regarding microvoids in this regime must be discarded.

SAXS Study of DTU Microcrystalline Films

We have analyzed two sets of films (4 each) supplied by Delft Technical University (DTU) that were prepared by expanding-thermal-plasma CVD (ETP CVD). The goal is to increase the deposition rate for μ c-Si:H solar cell material. The SiH_4 flow is varied to cover the transition from

amorphous to microcrystalline material. For the first film series the SiH_4 injection ring was positioned close to the plasma source exit at 365 mm above the substrate and for the second series it was placed much closer to the substrate at 55 mm. The deposition rates ranged from 0.91 to 1.52 nm/s. The eight films were measured by XRD before folding into 8 layers for SAXS. Figure 13 shows the XRD patterns, which are organized in terms of increasing crystallinity from bottom to top. The strong lines near $2\theta = 38^\circ$ and 44° are due to the Al-foil substrate. Using our procedure for determining the $\mu\text{c-Si}$ fraction, the values found are in good agreement with those from Raman spectroscopy done at DTU.

The microstructure of the eight Delft films prepared by ETP CVD, as determined by SAXS, are remarkably similar in spite of significant differences in the degree of crystallinity. For two samples which are fully amorphous according to XRD, the SAXS remains strong and comparable to the other samples with partial microcrystallinity. This suggests that the microcrystals do not contribute strongly to the SAXS. The SAXS and flotation density are consistent with void fractions near the 5 vol. % level. The flotation densities are somewhat larger in the second series of films utilizing smaller separation of SiH_4 injection and substrate positions, implying some improvement in the compactness of the films. However, the SAXS remains unusually strong, consistent with a high degree of heterogeneity in the films studied to date.

SAXS Study of UT Films Made from Disilane and Trisilane

Four films were provided by the University of Toledo (UT), two of which were made with disilane and the other two with trisilane, all with high hydrogen dilution to produce material near the amorphous/microcrystalline phase boundary. Films made under nominally identical conditions were made into solar cells to find V_{oc} . Both films made with trisilane were partially microcrystalline and showed strong SAXS, while one of the disilane films was fully amorphous and showed weak SAXS. There was a good V_{oc} correlation for all films but one [low V_{oc} (~ 0.87 V) if partially microcrystalline and high V_{oc} (~ 1.00 V) if fully amorphous]. This can be attributed to the thickness effect on microcrystallite formation (the SAXS films were thicker than the V_{oc} films) and a higher sensitivity of this effect when using trisilane. Again, the transition to partial microcrystallinity results in a sharp increase in film heterogeneity.

1.3.3 Wide-Angle X-ray Diffraction Experiments (Task 3)

XRD Study of USSC Partially Microcrystalline Solar Cells – V_{oc} Issue

Additional x-ray diffraction experiments have been made in collaboration with the USSC group in search of the mechanism for the light-induced increases in open circuit voltage, V_{oc} , in partially microcrystalline solar cells prepared just above the onset of microcrystallinity. Our first results were presented in the NREL final report from the previous subcontract. The two additional cell structures yielded the same *negative* result in that no changes were detected in the XRD patterns of the (220) peak before and after light soaking. These were done with care to position the sample in the same place in the XRD system and with very long counting times to obtain good statistics. No difference in microcrystalline fraction could be found to a precision of about 1 vol. %. Based on our earlier correlation of V_{oc} and partial microcrystallinity, changes of at least 5 vol. % could be expected for the ~ 100 mV changes in V_{oc} if this was indeed the mechanism.

XRD Study of USSC Microcrystalline Solar Cells – Deposition Effects

A set of seven samples of microcrystalline solar cells was supplied by USSC for investigation by XRD at CSM. They were made by RF-, VHF-, and MW-PECVD, representing low, intermediate, and high deposition rates, respectively. The goal was to look for correlations of device behavior (ambient stability, J_{sc}) and structural factors determined by XRD (film texture, grain size, lattice parameters, degree of crystallinity). The following correlations with cell behavior were observed: (a) both samples with the highest “degree of crystallinity” have “ambient unstable” behavior; (b) two VHF samples both have “high J_{sc} , ambient stable” behavior and have quite similar XRD parameters; (c) on the other hand, a third VHF sample has similar parameters to these, yet yields “low J_{sc} ”. [The latter sample does have the highest lattice expansion (most compressive stress) of the set]; the microwave sample (highest deposition rate) has the smallest grain sizes and least “degree of crystallinity”, likely correlating with the “low J_{sc} ”. The RF sample seems to stand out with the strongest preferred (220) texture, and this may be correlated with the “high J_{sc} , ambient stable” behavior.

Table of Contents

1. Executive Summary	i
1.1 Preface	i
1.2 Objectives/Approach	i
1.3 Conclusions	i
List of Figures	ix
List of Tables	x
2. Introduction	1
3. Results and Discussion	2
3.1 Transmission Electron Microscopy Experiments (Task 1) ..	2
3.1.1 Experimental Details	2
3.1.2 XTEM Study of a-Si:H and a-Si:D Solar Cell Material	3
3.1.3 XTEM Study of a-SiGe:H Alloys	12
3.1.4 XTEM Study of Nano- and Microcrystalline-Si Solar Cells and Materials	17
3.2 Small-Angle Scattering Experiments (Task 2)	25
3.2.1 SANS Quantitative Interpretation	25
3.2.2 SAXS Study of BP-Solar a-Si:H Deposition Rate Series	25
3.2.3 SAXS Study of HWCVD a-SiGe:H Alloys	27
3.2.4 SAXS Study of HWCVD a-Si:H Deposited at High Rate with H Dilution	30
3.2.5 SAXS Study of USSC Microcrystalline Solar Cell Materials	32
3.2.6 SAXS Study of KAIST Photo-CVD a-Si:H Films	36
3.2.7 SAXS Study of DTU Microcrystalline Films	44
3.2.8 SAXS Study of UT Films Made from Disilane and Trisilane	52
3.3 Wide-Angle X-ray Diffraction Experiments (Task 3) ..	56
3.3.1 XRD Study of USSC Partially Microcrystalline Solar Cells – V_{oc} Issue	56
3.3.2 XRD Study of USSC Microcrystalline Solar Cells –Deposition Effects	57
4. Acknowledgements	61
5. References	61

List of Figures

Fig. 1. XTEM images of a-Si:H solar cell material prepared under high H ₂ dilution.	4
Fig. 2. XTEM images of a-Si:H film from the a-Si film/Si substrate interface area.	5
Fig. 3. XTEM images from a HWCVD a-Si:H film prepared at ultra-high deposition rate . . .	6
Fig. 4. XTEM image from a HWCVD a-Si:H film prepared at ultra-high deposition rate	7
Fig. 5. XTEM images of Si:D solar cell material	9
Fig. 6. XTEM images from different areas of Si:D solar cell material	10
Fig. 7. High resolution XTEM image showing some ordering in the amorphous Si:D	11
Fig. 8. Bright-field XTEM image from the overall HWCVD a-SiGe:H film	13
Fig. 9. XTEM images of different areas from a-SiGe:H film	14
Fig. 10. XTEM image showing a large area from a-SiGe:H film	15
Fig. 11. XTEM images of different areas from a-SiGe:H film	16
Fig. 12. XTEM images of a nanocrystalline Si solar cell on Asahi TCO.	18
Fig. 13. XTEM images of a nanocrystalline Si solar cell on textured ZnO.	19
Fig. 14. XTEM images of the microstructure of the nanocrystalline Si layer of Sample 7.	21
Fig. 15. XTEM images of the microstructure of polycrystalline Si film on Al-coated glass. . .	23
Fig. 16. XTEM images of the microstructure of NREL microcrystalline Si film on c-Si	24
Fig. 17. SAXS data and fits for the six BP-Solar films	26
Fig. 18. IR data from four BP-Solar films	27
Fig. 19. SAXS integrated intensities from HWCVD a-SiGe:H series of alloys	28
Fig. 20. SAXS from HWCVD a-SiGe:H alloys with different filament temperatures	29
Fig. 21. Correlation of SAXS integrated intensity and photoconductivity for a-SiGe:H alloys. .	30
Fig. 22. SAXS data from NREL HWCVD a-Si:H made with H dilution	31
Fig. 23. SAXS data from three USSC microcrystalline-Si:H films	33
Fig. 24. XRD patterns from three USSC microcrystalline-Si:H films	35
Fig. 25. XRD patterns from KAIST films with increasing R	37
Fig. 26. SAXS data from all KAIST films	39
Fig. 27. SAXS R=0.5 data, fit to data, and model calculations for spherical voids	40
Fig. 28. SAXS R=2.0 data, fit to data, and model calculations for spherical voids	41
Fig. 29. SAXS R=3.0 data in non-tilted and tilted orientations	42

Fig. 30. XRD patterns from two series of DTU samples	46
Fig. 31. SAXS data from two series of DTU samples	48
Fig. 32. Examples of fits of size distributions of spheres to DTU sample #1	50
Fig. 33. XRD patterns from UT samples on Al foil substrates	53
Fig. 34. SAXS data from the UT samples. Comparison data from USSC film	54
Fig. 35. XRD from $\mu\text{c-Si}$ cell sample RF11486 compared to Ag/ZnO-coated SS reference . . .	58
Fig. 36. XRD scans of USSC cell samples over the (111) and (311) peak regions of c-Si	59

List of Tables

Table 1. a-Si XTEM samples, preparation, and composition	3
Table 2. a-SiGe:H XTEM samples, preparation, and composition	13
Table 3. Microcrystalline Si XTEM samples, preparation, and composition	17
Table 4. Results from IR, SAXS, and flotation density studies of BP-Solar a-Si:H films	26
Table 5. HWCVD preparation conditions for SAXS samples using hydrogen dilution.	31
Table 6. Quantitative SAXS results from hydrogen diluted HWCVD films	32
Table 7. Preparation and composition of USSC $\mu\text{c-Si}$ films for SAXS	32
Table 8. SAXS and flotation density results from microcrystalline films of USSC.	34
Table 9. XRD results from USSC $\mu\text{c-Si}$ films.	34
Table 10. Summary of properties of KAIST films provided	36
Table 11. Quantitative SAXS results and flotation densities for KAIST films	43
Table 12. XRD results from DTU series of $\mu\text{c-Si}$ films	45
Table 13. SAXS quantitative results and flotation densities from DTU series of $\mu\text{c-Si}$ films . .	49
Table 14. Preparation and V_{oc} data for UT SAXS films and solar cells	52
Table 15. SAXS quantitative results and flotation densities for UT films	55
Table 16. USSC $\mu\text{c-Si}$ samples, preparation conditions, and cell behavior	57
Table 17. Quantitative XRD analysis results from USSC $\mu\text{c-Si}$ solar cell i-layers	60

2. INTRODUCTION

This purpose of this subcontract, as part of the R&D Partner Category, is to achieve a better understanding and to improve the materials used as the intrinsic layers of silicon-based solar cells. Fundamental structural properties will be investigated on atomic- and nano-scales. Cell performance and light-induced degradation in these materials seem to depend critically on the microstructure of the films and the presence of heterogeneities such as microvoids, H-rich areas, reduced density areas, and Ge composition fluctuations in the alloy films. A powerful combination of techniques will be used: analytical high-resolution transmission electron microscopy (HRTEM), including special associated spectroscopic methods, small-angle and wide-angle scattering techniques, including x-rays (SAXS, XRD), neutrons (SANS) and anomalous x-rays (ASAXS). The work will build on extensive prior experience with the latter two techniques, which have provided new and detailed structural information on state-of-the-art solar-cell materials and other thin-film materials during the last few years [1].

The addition of HRTEM will provide direct imaging of the microstructure of the intrinsic layer materials as well as of actual complete solar cell devices. HRTEM is expected to provide direct images of many of the structural defects and features that have been identified by the x-ray and neutron scattering techniques in our previous research. Measurements by both methods on the same or co-deposited films will be a key feature of the experimental approach. An innovative combination of high-resolution imaging and electron energy loss spectrometry (EELS), energy-loss near-edge structure (ELNES) and extended energy-loss fine structure (EXELFS) in a TEM, will address issues of particular importance, such as: (i) fluctuation of Ge composition in low-gap a-SiGe alloys identified by ASAXS, (ii) the detailed nature of highly elongated and oriented scattering features, as well as nano-sized microvoids identified by SAXS, and (iii) atomic-scale ordering, bonding and coordination of the most stable a-Si:H prepared “on the edge” of microcrystallinity.

A key advantage of SANS in comparison to SAXS is the much-improved sensitivity to the location of the hydrogen. High-flux neutron facilities, dedicated to SANS research, are available at the National Institute of Standards and Technology (NIST), in Gaithersburg, Maryland, and we already have considerable experience in access and use of this facility and have demonstrated the viability of this technique for the thin-film materials of interest here.

Another special small-angle scattering technique that will continue to be utilized in this project is anomalous SAXS (ASAXS), available through collaboration with a group in Germany at the DESY

synchrotron in Hamburg. This method is ideally suited to search for non-uniform Ge distributions in a-SiGe:H alloys and data obtained under current funding shows good evidence for a non-random Ge distribution in both PECVD and HWCVD films. This characteristic could be related to the currently unavoidable degradation of opto-electronic properties with Ge alloying, particularly for bandgaps near and below 1.4 eV.

The principal goal of this project will be to provide relevant structural information to NREL supported groups that are developing new materials, new deposition methods, and optimizing existing materials in the quest for improved materials and the achievement of the 15% stabilized efficiency for thin-film a-Si modules. This research group at the Colorado School of Mines will continue participating in National R&D Team activities.

Several experiments have been completed during Phase I of this research project in collaboration with NREL and NREL-supported groups, as well as with other groups having expertise in the field of amorphous and microcrystalline silicon-based solar-cell materials. The results and discussion will be presented in three sections corresponding to the three main tasks: (1) Electron microscopy experiments, (2) small-angle scattering experiments, and (3) wide-angle x-ray diffraction experiments.

3. RESULTS AND DISCUSSION

3.1 Transmission Electron Microscopy Experiments (Task 1)

Here we describe our use of cross-sectional transmission electron microscopy (XTEM) to investigate the microstructure of a-Si:H and a-SiGe:H films as well as nano-crystalline/microcrystalline-Si films and devices prepared by both plasma-enhanced and hot-wire chemical vapor deposition.

3.1.1 Experimental details

All the TEM cross-sectional specimens (total of 10) were prepared using tripod polishing. This method is particularly suitable for the preparation of large homogeneously thin electron transparent regions. The mechanical polishing step yields samples thinned to below 50 nm. This step is followed by very brief (~10 minutes) ion-milling in a BalTec Res 100 ion mill at a sputtering angle of 4 degrees to minimize any structural modifications due to specimen preparation. The samples were examined in a Philips CM200 transmission electron microscope operating at 200 kV.

3.1.2 XTEM Study of *a*-Si:H and *a*-Si:D Solar Cell Materials

Two different *a*-Si:H films and one *a*-Si:D film have been investigated using XTEM. The sample numbers and some details of their preparation are given in Table 1. Infrared spectroscopy was used to obtain bonded H contents in the samples. Below representative XTEM images will be presented along with major observations for each sample.

Table 1. *a*-Si XTEM samples, preparation, and composition.

Sample No.	Sample I.D.#	Preparation	[H] at%	[D] at. %
1	USSC-R8463	PECVD of SiH ₄ with high H ₂ dilution	11	0
2	NREL-T1777/78	HWCVD of SiH ₄ at 10 nm/s	8	0
3	USSC-R8468	PECVD of SiD ₄ with high D ₂ dilution	1	13

The results of the XTEM investigation of the *a*-Si:H solar cell material (Sample 1) are shown in Figure 1 [2]. An XTEM image of the overall film with a thickness of $\sim 2 \mu\text{m}$ is shown in Figure 1A. The *a*-Si:H film shows homogeneous contrast apart from an initial epitaxial crystalline interface layer ($\sim 200\text{--}250 \text{ nm}$) adjacent to the Si (100) substrate. Also, the lack of any (111), (220), or (311)

XRD peaks is consistent with the epitaxial nature of the initial film growth [3]. Electron diffraction in the TEM as well as X-ray diffraction [3] confirm that the Si:H material is amorphous. Well-pronounced strain-contrast is observed in the crystalline Si substrate, consistent with the high compressive stress in such films [3]. Figures 1B and 1C represent higher magnification images from regions close to the top surface of the film (Figure 1B) and to the film – substrate interface (Figure 1C). These XTEM images confirm that away from the substrate/film interface the film becomes completely amorphous and uniformly dense. Most importantly, the uniformity is characteristic of the whole film; there is no evidence of microvoids or mass density fluctuations. This homogeneity is in good agreement with the SANS results from this sample [3]. At higher magnification some evidence of ordering on the nanoscale in the amorphous phase, similar to the ‘chain-like objects’ [4] can be seen, Figure 2. In the insert in Figure 2 an image of fully amorphous

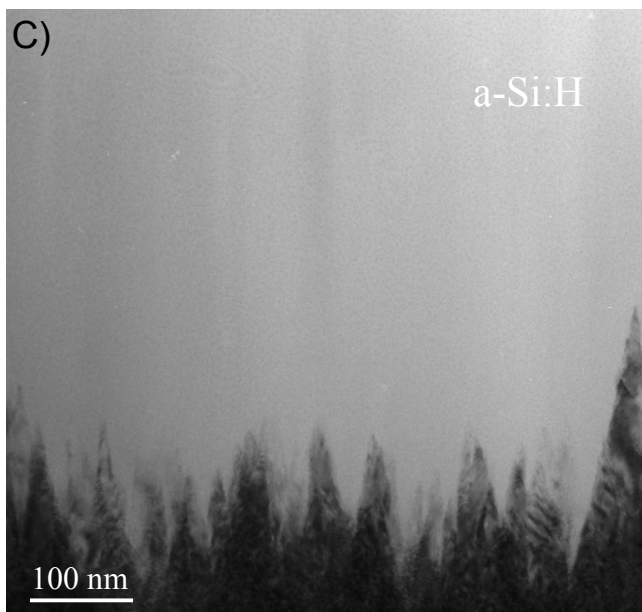
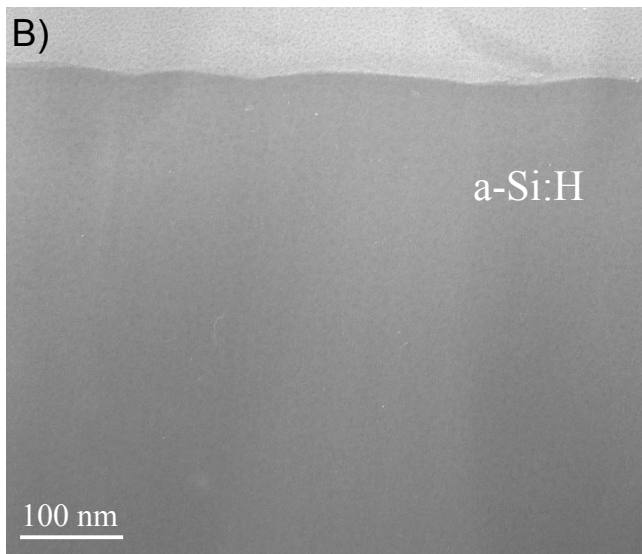
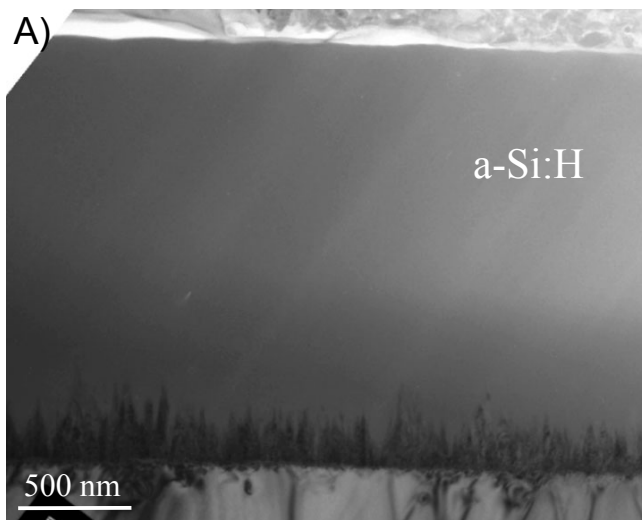


Figure 1. XTEM images of a-Si:H solar cell material prepared under condition of high H_2 dilution on Si(100) substrate (Sample 1, Table 1). 1A) Cross-section of the entire film; 1B) detail from the area close to the top surface; 1C) detail from the a-Si film/Si substrate interface.

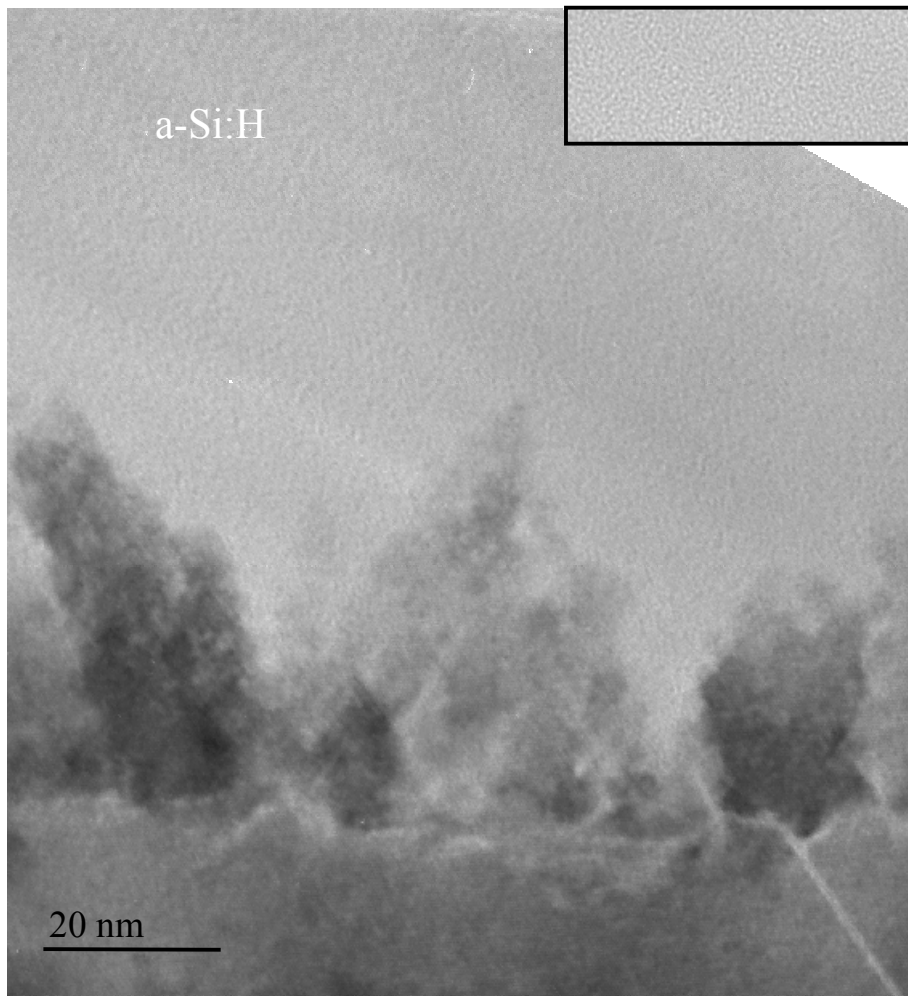


Figure 2. XTEM images of a-Si:H film(Sample 1, Table1) from the a-Si film/Si substrate interface area. Close to the crystalline regions some ordering in the amorphous material is present. The insert shows fully amorphous material for comparison.

material without ‘chain-like’ ordering is included for comparison. It is worth noting that such somewhat ordered areas are observed always close to crystalline areas, in this sample close to the crystalline interlayer at the film/substrate interface.

Figure 3A shows a bright-field XTEM micrograph of the overall a-Si:H film prepared by HWCVD at very high deposition rate (Sample 2). The film shows homogeneous contrast and this together with electron diffraction in the TEM and XRD [1] indicates that the material is amorphous and there is no change in *crystallinity* over the thickness of the film. Higher magnification TEM images of the amorphous microstructure of this film show, nevertheless, significant heterogeneity. XTEM images of the microstructure from different areas of the film are shown in figure 3B and 3C. Figure 3C is a high-resolution image of the a-Si:H film/c-Si substrate interface. The XTEM

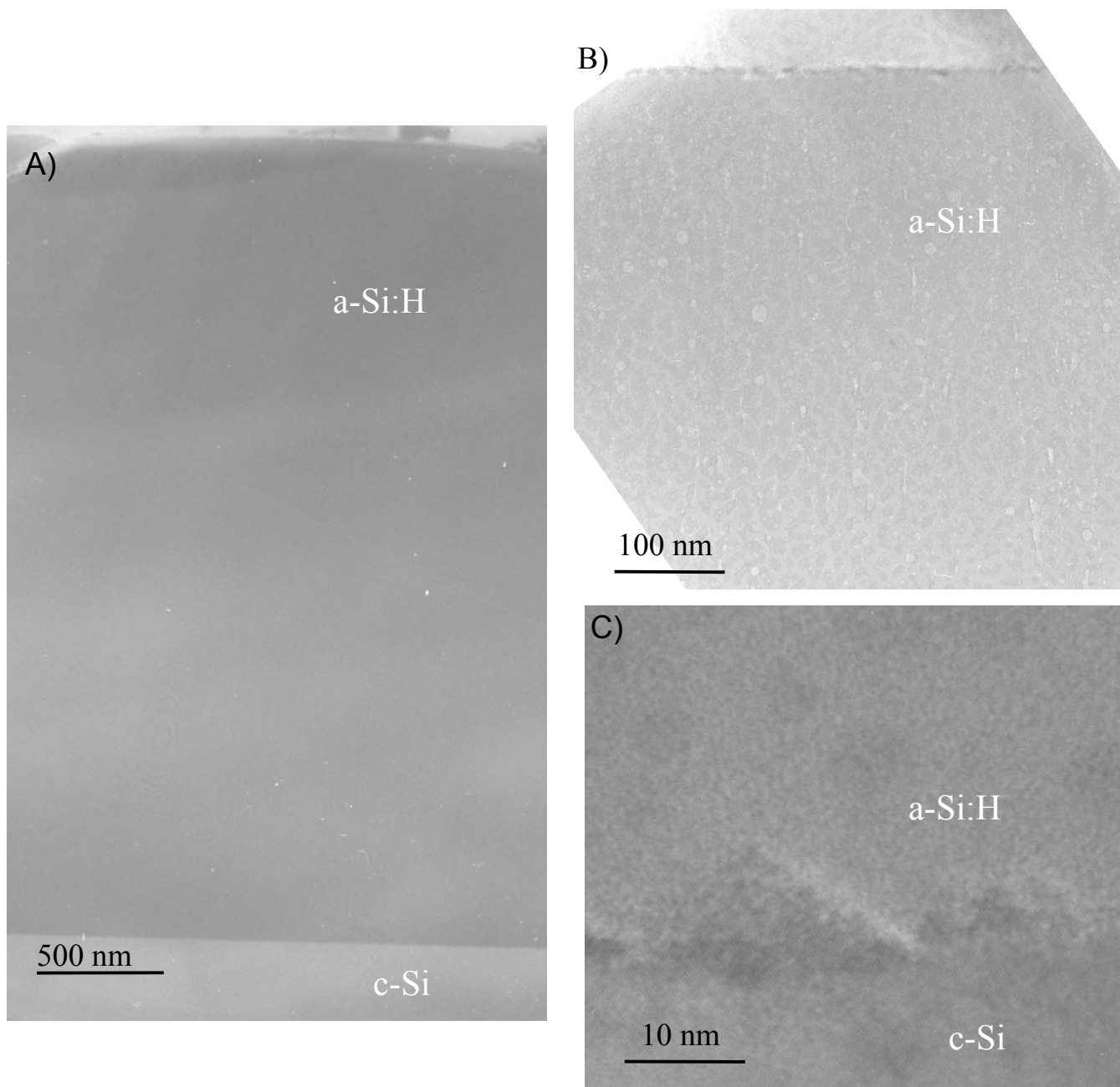


Figure 3. Bright-field XTEM images from a HWCVD a-Si:H film prepared at ultra-high deposition rate (Sample 2, Table1). 3A) Overall microstructure; 3B) area close to the top surface of the film; 3C) high-resolution image of the a-Si:H film/c-Si substrate interface.

micrograph reveals the presence of a crystalline interface layer with a thickness of ~ 10 nm. The a-Si:H material close to the interface is seen to be amorphous and structurally homogeneous. Figure 3B and Figure 4 (imaging a larger area of Sample 2) shows a region of the a-Si:H material away from the film/substrate interface which appears amorphous but it does not appear structurally

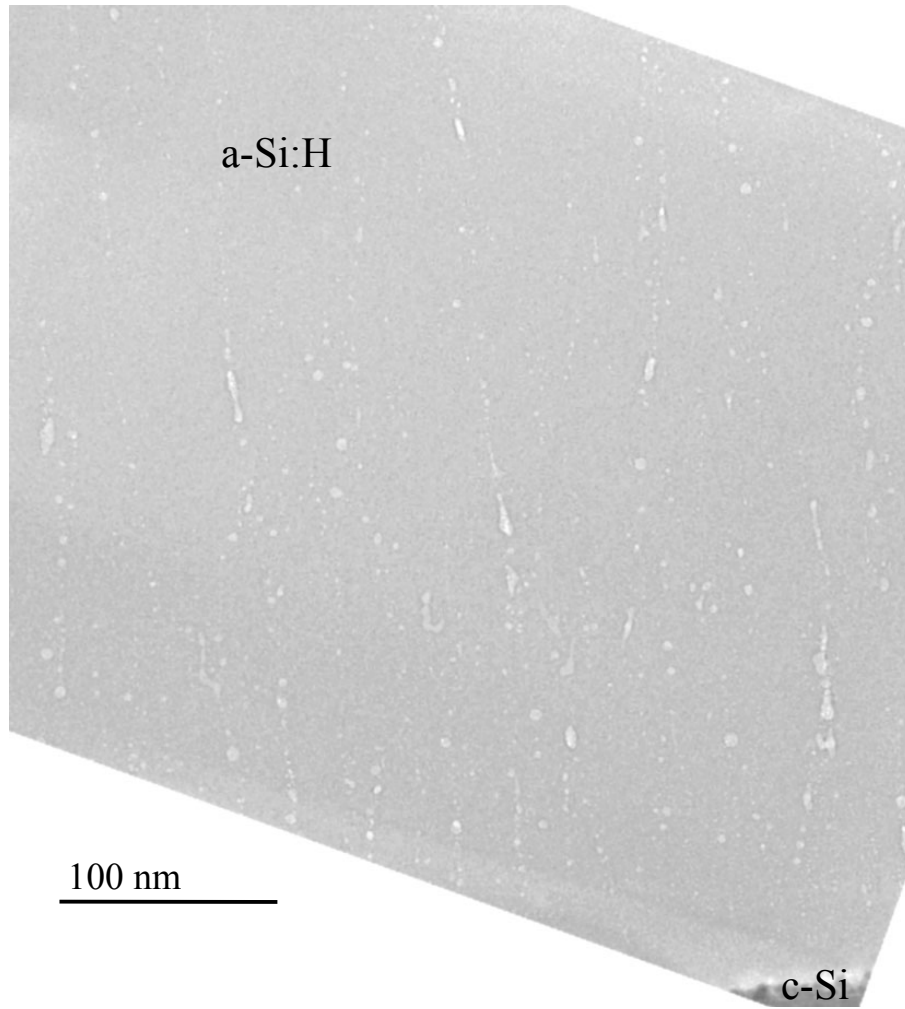


Figure 4. Bright-field XTEM image from a HWCVD a-Si:H film prepared at ultra-high deposition rate (Sample 2, Table1) showing structural non-uniformity.

homogeneous. The contrast stemming from the a-Si:H material is not uniform. Well-defined spherical as well as slightly elongated in shape features can be observed. Given that mass-thickness contrast is mainly responsible for image formation in bright-field TEM imaging of amorphous structures we can attribute regions with lighter contrast to reduced density. The features observed here appear to be mainly due to the presence of microvoids. The structural inhomogeneity features ('microvoids') are observed through the whole thickness of the a-Si:H film. Figure 3B, which is a TEM micrograph from the region close to the surface of the film, shows that the spherical as well as slightly elongated features are present here as well. They terminate at the surface of the film. It should be mentioned that no noticeable clustering or change of the distribution of the 'microvoids' is observed throughout the film. The sizes of the features, ~ 5 nm in the film plane, and their

oriented, elongated nature is consistent with the SAXS [5] and SANS [6] analyses of this type of a-Si:H.

The results of the XTEM investigation of the a-Si:D solar cell material [2] (Sample 3) are shown in Figure 5. The deuterated a-Si film (Sample 3) was prepared as a matched pair with the hydrogenated a-Si (Sample 1) [3]. They were deposited using PECVD under conditions similar to those that have yielded record high efficiency solar cells [3, 7]. The only difference in preparation other than the source gas used (in the case of the Si:H sample – a combination of SiH_4 and H_2 , and in the case of the Si:D sample - SiD_4 and D_2) was a somewhat higher plasma power for the a-Si:D film (1.46 times that used for the a-Si:H film). This was done in order to produce similar deposition rates: 0.13 nm/s for the a-Si:H and 0.14 nm/s for the a-Si:D material. Both samples were deposited under conditions of ‘high dilution’.

Figures 5 A and B show bright-field XTEM micrographs of the overall structure of Sample 3 - Si:D film ($\sim 2 \mu\text{m}$ thick) on the Si (100) substrate. In contrast to the a-Si:H material (Figure 1, Sample 1) this film is non-homogeneous. The deuterated Si film represents a heterogeneous mixture of amorphous and microcrystalline Si. A significant amount of the crystalline material is located close to the substrate but crystalline regions are observed throughout the whole thickness of the film. Figure 5 clearly indicates that the presence of crystalline regions is not the only source of heterogeneity in this film. The amorphous matrix is not homogeneous as well – a significant amount of low-density (deuterium-rich) regions or microvoids, or possibly both are clearly seen. The detailed evolution with thickness of the microstructure of the deuterated Si film can be followed in Figure 5B. The growth of the Si:D film starts epitaxially, similar to the a-Si:H film. In the Si:D film the interlayer material appears very dense with individual grains reaching up to ~ 200 - 300 nm in size. Certain ‘crystalline needle-like’ grains reach a length of up to $1 \mu\text{m}$. Apart from the ‘crystalline needle-like’ grains, as the growth continues away from the film/substrate interface, formation of amorphous Si:D is observed. As mentioned above the amorphous material is not homogeneous and uniform but shows the presence of D-rich regions/microvoids. These regions are observed to have two distinct shapes: spherical and elongated, with a preferred elongation in the film plane (‘in-plane’). In the top part of the deuterated film, the presence of microcrystalline material in the form of grains dispersed through the amorphous matrix is observed as well. These are found to have predominantly (111), (110) and (311) orientation. The (110)-oriented grains appear to grow fast and develop into cone-like shape. One such case of grain evolution is seen near

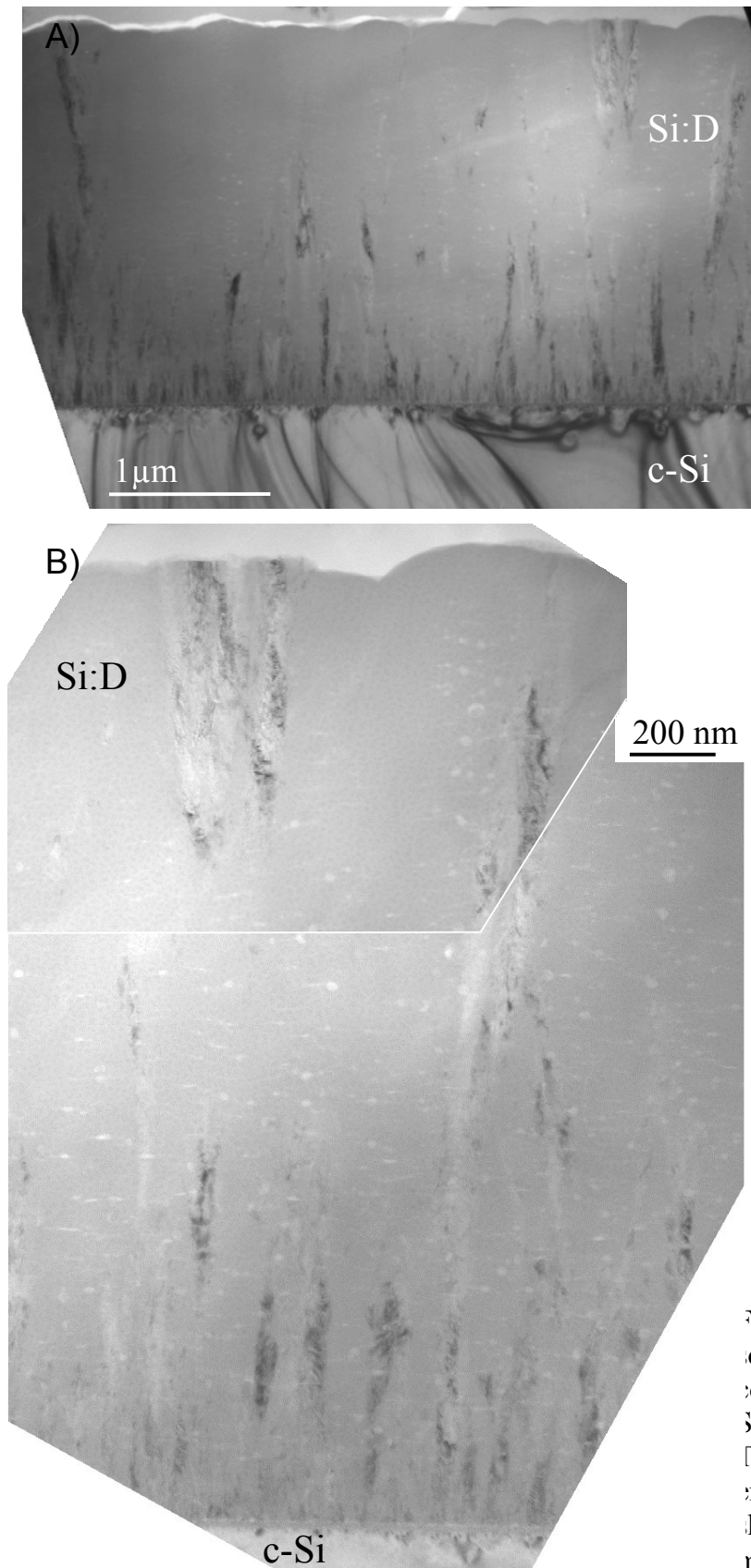


Figure 5. XTEM images of Si:D solar cell material prepared under condition of high D_2 dilution on Si(100) substrate (Sample 3, Table1). 5A) Cross-section of the entire film; 5B) detailed image showing the evolution of the microstructure.

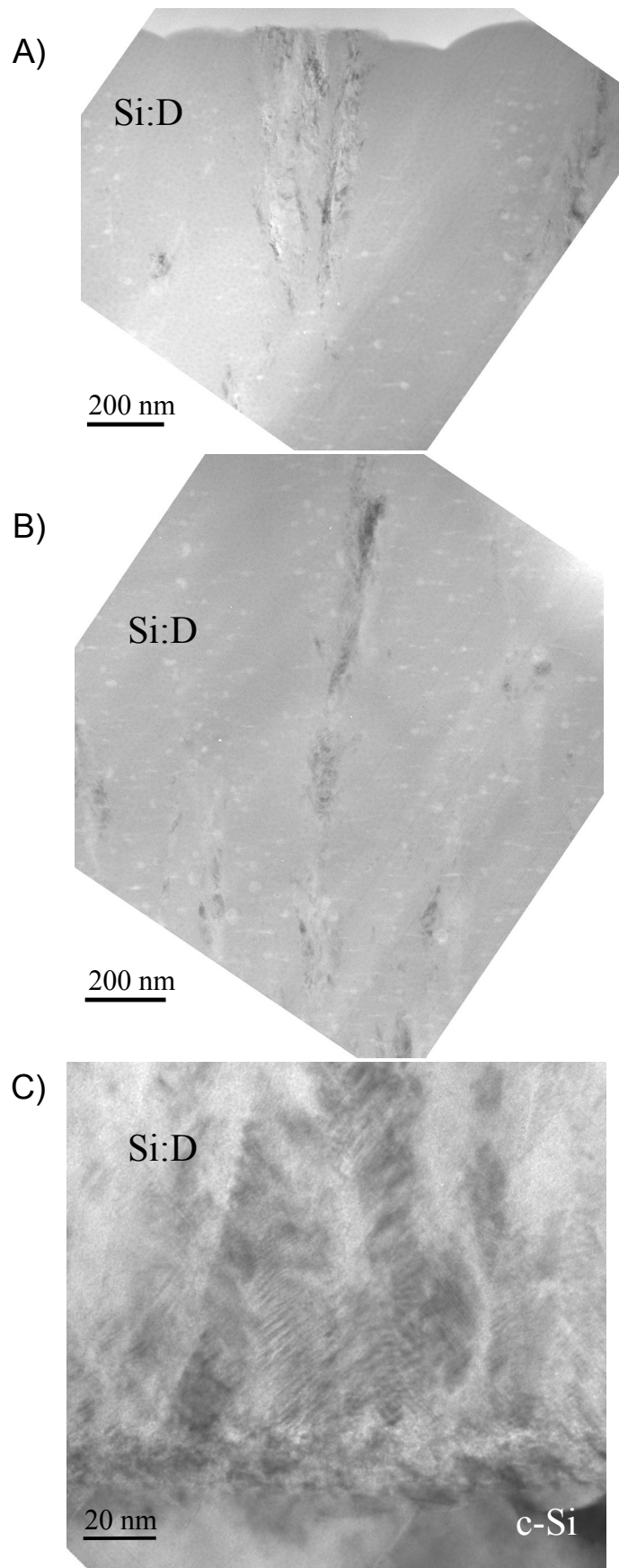


Figure 6. XTEM images from different areas of Si:D solar cell material prepared under condition of high D_2 dilution (Sample 3, Table1). 6A) Close to the surface; 6B) mid section of the film; 6C) initial stage adjacent to the substrate.

the top of Figure 5B. These grains seem to grow faster than the amorphous material resulting in an increase in surface roughness in the deuterated Si film compared to the hydrogenated one, consistent with the AFM results in [3]. It should also be noted that the density of D-rich regions/microvoids is higher close to the crystalline needles. Away from the crystalline areas the amorphous matrix less D-rich regions/microvoids are observed. The evolution of the microstructure of Sample 3 is shown in somewhat more detail in Figure 6. This figure shows images from different areas of the film along the growth direction: Figure 6A – close to the surface, Figure 6B – the mid section of the film, Figure 6C – the initial stage of formation adjacent to the substrate. Similar to Sample 1, prepared under high hydrogen dilution, in the deuterated material (Sample 3) evidence for ordering on the nanoscale was found. Figure 7 presents a high-resolution XTEM image where ‘chain-like objects’ can be seen. Similar to Sample 1 these more ordered areas are observed only close to crystalline areas in the film.

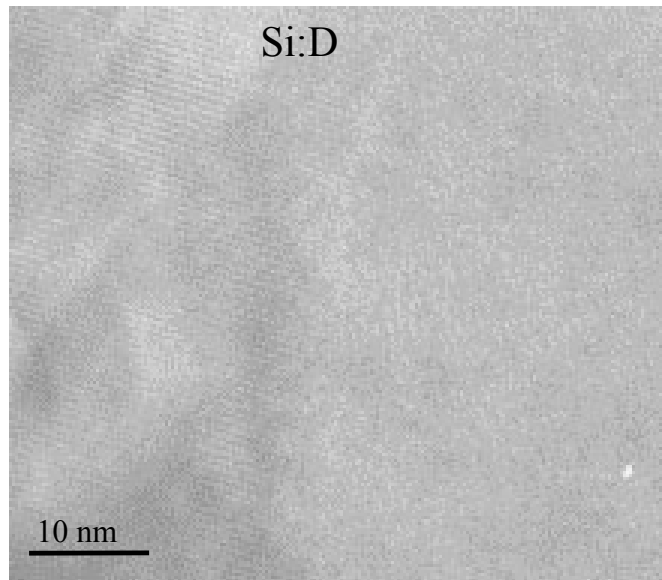


Figure 7. High resolution XTEM image showing some ordering in the amorphous Si:D close to a crystalline grain in Si:D solar cell material prepared under condition of high D₂ dilution (Sample 3, Table1).

The XTEM investigation of the hydrogenated and deuterated Si solar cell material prepared under condition of high H₂ and D₂ dilution, respectively, provides direct observation and comparison of the microstructure of the two materials. The hydrogenated Si material appears uniform and contains no microvoids, in agreement with earlier studies [3]. In contrast, the

deuterated Si material represents a heterogeneous mixture containing amorphous matrix, ‘crystalline needle-like’ grains, randomly nucleated grains in the top half of the film, and D-rich regions/microvoids. It has been established that depositing Si under conditions of sufficiently high hydrogen dilution results in formation of microcrystalline material. The comparison of the results in Figures 1 and 5 indicate that the replacement of hydrogen with deuterium is equivalent to an effective increase in dilution promoting crystalline material formation. This is probably due to the more efficient transfer of momentum and energy from the heavier deuterium in this plasma enhanced process. The somewhat higher plasma power used to deposit the deuterated film might further enhance this efficiency. A simultaneous process that leads to enhancement of the crystalline content is the etching of the surface that becomes prominent under conditions of heavy dilution with deuterium in particular [7].

Following the evolution of the microstructure of the deuterated Si film provides an insight into the effect of deuterium on this microstructure. As mentioned above the amorphous matrix is not homogeneous but it contains D-rich regions/microvoids that are moreover not uniformly dispersed but have higher density close to the crystalline grains. It is reasonable to assume that the deuterium gets partially incorporated into the microcrystalline Si. This assumption is supported by shifts in the XRD line attributed to high compressive stress [9]. Once the solubility threshold is exceeded excess deuterium is expelled into the adjacent amorphous matrix where it aggregates. This in combination with the high compressive stress probably causes the ‘in-plane’ elongation of the D-rich regions/microvoids. The ‘in-plane’ elongation is in contrast to the elongation along the growth direction associated previously with residual columnar-like structure [1]. Rather, the deuterium seems to move away from the crystallites and precipitate to form the D-rich regions/microvoids. These low-density features have characteristic size $\sim 8 - 15$ nm, which identifies them as the likely source of additional SANS scattering observed earlier [3].

3.1.3 XTEM Study of a-SiGe:H Alloys

Two different a-SiGe:H films have been investigated using XTEM. The sample numbers and some details of their preparation are given in Table 2. Infrared spectroscopy was used to obtain bonded H contents in the samples and electron microprobe measurements provided the Ge fraction x in the a-Si_{1-x}Ge_x:H alloys. Below representative XTEM images will be presented along with major observations for each sample.

Table 2. a-SiGe:H XTEM samples, preparation, and composition.

Sample No.	Sample I.D.#	Preparation	Ge (x)	[H] at. %
4	NREL-T1780/81	HWCVD of SiH ₄ +GeH ₄	0.15	3
5	USSC-R8479	PECVD of SiD ₄ +GeD ₄	0.40	13

Figure 8 shows a bright-field XTEM micrograph of the overall a-SiGe:H film on Si substrate (Sample 4). The film shows homogeneous contrast and this together with electron diffraction in the TEM indicates that the material is amorphous and there is no change in *crystallinity* over the thickness of the film. The thickness of the film is $\sim 2.35 \mu\text{m}$.



Figure 8. Bright-field XTEM image from the overall HWCVD a-SiGe:H film (Sample 4, Table2).

Higher magnification TEM images of the microstructure from different areas of the film are shown in figure 9. Figure 9A is an image of the a-SiGe:H film/Si substrate interface. The XTEM micrograph reveals the presence of a polycrystalline interface layer with a thickness of ~ 20 nm. Figure 9B shows a region of the a-SiGe:H material close to the film/substrate interface. The a-SiGe:H material appears amorphous but it does not appear structurally homogeneous. The contrast stemming from the a-SiGe:H material is not uniform. Slightly elongated (close to spherical) features can be observed. Similar to the heterogeneity in samples 2 and 3, here we can attribute regions with lighter contrast to reduced density, microvoids, or composition fluctuations (H and/or Ge fluctuations). Higher magnification imaging from a region away from the interface shows the same non-uniform contrast (Figure 9C). The structural inhomogeneity features undergo a change from almost spherical at the film/substrate interface to highly elongated with increasing the thickness of the a-SiGe:H film. The features appear to be highly elongated along the film growth

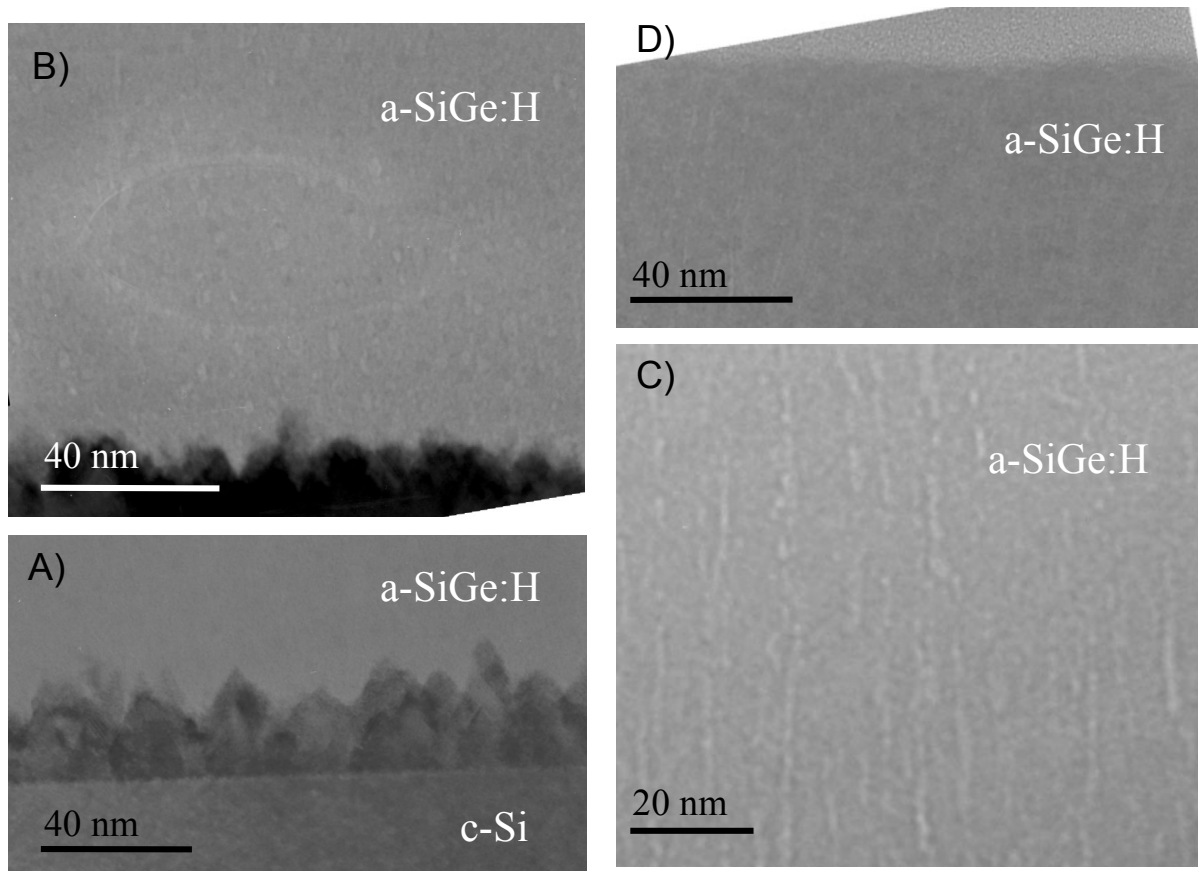


Figure 9. XTEM images of different areas from a-SiGe:H film (Sample 4, Table 2). 9A) The a-SiGe/c-Si substrate interface; 9B) close to the film/substrate interface; 9C) middle of film; and 9D) top surface of the film.

direction. The lateral size of the features is $\sim 1-2$ nm. Figure 9D shows a TEM micrograph from the region close to the surface of the film. The elongated features are present in it as well. They terminate at the surface of the film. Figure 10 shows a large area from the a-SiGe:H material. The micrograph demonstrates the presence and even distribution of high density of highly-elongated, low-density features in the material. Such features have long been implied by SAXS [1, 8] but never observed directly to our knowledge.



Figure 10. XTEM image showing a large area from a-SiGe:H film (Sample 4, Table 2).

Figure 11A shows a bright-field XTEM micrograph of the overall a-SiGe:H film on Si substrate (Sample 5) prepared by PECVD. The film shows homogeneous contrast stemming from its amorphous nature and no change in crystallinity is observed over the thickness of the film. Higher magnification TEM images of the microstructure from different areas of the film are shown in figures 11B and 11C. Figure 11B is an image of the area close to the a-SiGe:H film/Si substrate interface. The XTEM micrograph reveals the presence of a defective interface layer with a thickness of ~ 20 nm showing the presence of dislocations. The a-SiGe:H material adjacent to the interface appears amorphous and structurally homogeneous. Away from the interface the a-SiGe:H

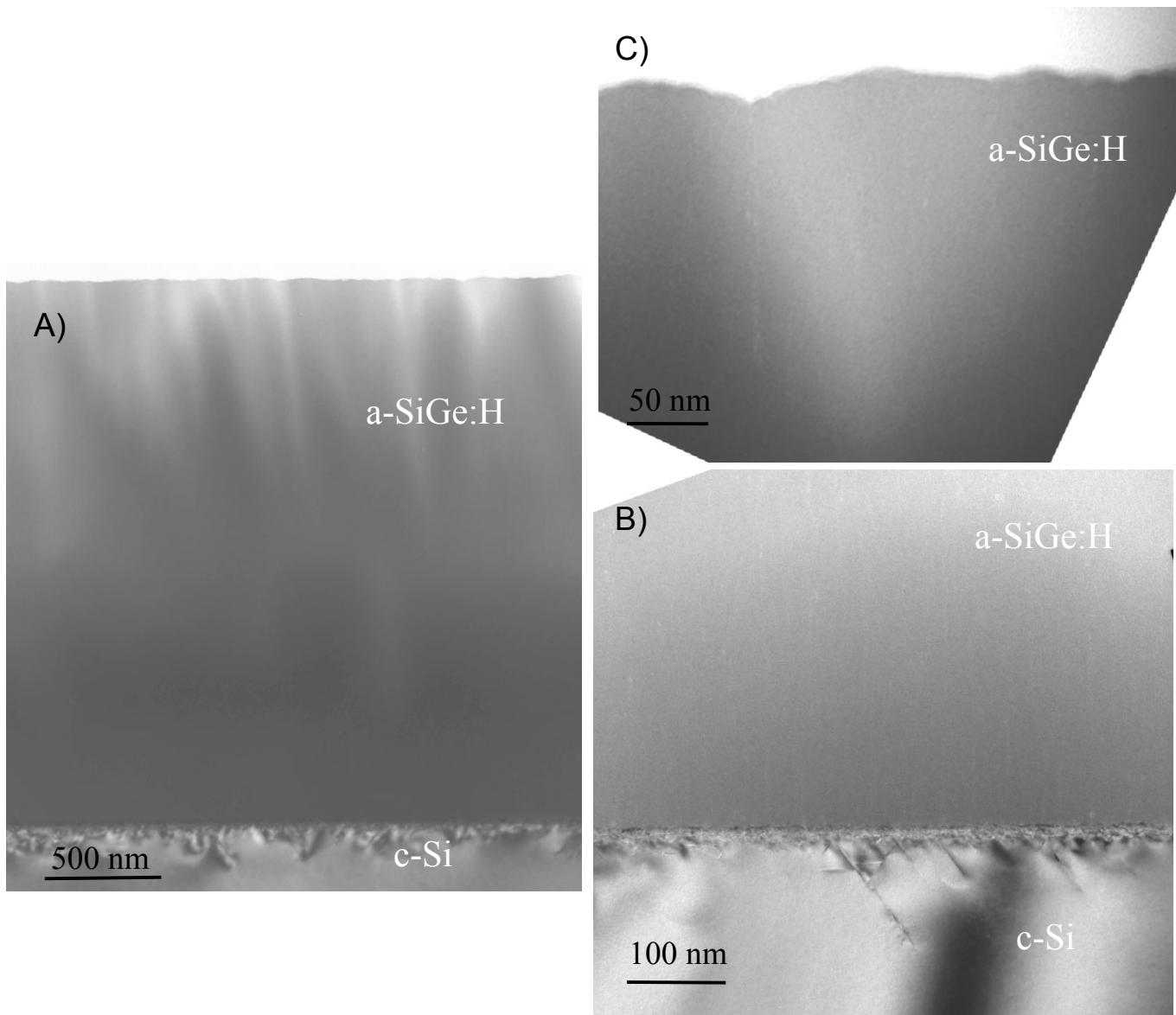


Figure 11. XTEM images of different areas from a-SiGe:H film (Sample 5, Table 2). 10A) Overall microstructure; 10B) close to the film/substrate interface; 10C) near the top surface of the film.

material is to a large extent homogeneous, however some non-uniformity in the contrast stemming from the a-SiGe:H material is observed. Slightly elongated-in-shape features can be seen. As noted above this is probably due to microvoids, H-rich areas, or (in these alloys) Ge composition fluctuations. The structural inhomogeneity features are present throughout the whole film and can be seen to propagate to its surface (Figure 11C). The features appear to be highly elongated along the film growth direction. Figure 11C shows a TEM micrograph from the region close to the surface of the film. The elongated features are present in it as well and terminate at the surface of the film. It can be seen that the area in which they terminate at the surface of the film corresponds

to a trough associated with the surface roughness. This is consistent with the SAXS interpretation of ‘residual columnar-like microstructure’ based on tilting effects showing anisotropic scattering from such alloys [8].

It is worth comparing the two a-SiGe:H films (Samples 4 & 5) presented here. Both films are amorphous and both show the presence of elongated-in-shape non-uniform features. In Sample 5, though, the amount of such features is significantly less and the a-SiGe:H material appears to be more uniform. This is consistent with SAXS/ASAXS/SANS evidence that the PECVD a-SiGe:H material is typically more homogeneous than the HWCVD alloys. However, as described below, new HWCVD alloys prepared with lower filament and substrate temperatures have much reduced heterogeneity.

3.1.4 XTEM Study of Nano- and Microcrystalline-Si Solar Cells and Materials

Five different nano- and microcrystalline Si films have been investigated using XTEM. Two of the samples were solar cell devices deposited on glass with different TCO layers (Samples 6 & 7); one was deposited on Al-coated glass substrate (Sample 8) and the remaining two were microcrystalline Si films deposited on crystalline Si (100) (Samples 9 & 10). The sample numbers and some details of their preparation are given in Table 3. Below representative XTEM images will be presented along with major observations for each sample.

Table 3. Microcrystalline Si XTEM samples, preparation, and composition.

Sample No.	Sample I.D.#	Preparation	Device efficiency [%]	Substrate
6	MVSystems-NRCT 954	PECVD of SiH ₄	6.8	Asahi TCO on glass
7	MVSystems-NRCT 1126	PECVD of SiH ₄	~ 8	Textured ZnO (AIST) on glass
8	IEC	HWCVD of SiH ₄	N/A	Al-coated glass
9&10	NREL 2399 & 2409	RTSE chamber SiH ₄ +H ₂	N/A	Si(100)

Figure 12 shows XTEM images from a nanocrystalline Si (nc-Si) solar cell deposited on Asahi TCO on glass substrate (Sample 6). In Figure 12A two layers can be clearly identified: the TCO adjacent to the substrate and the nc-Si on top. The TCO has a thickness ~ 750 nm, the nc-Si ~ 850 nm. The image of the TCO layer (Figure 12B) shows that it is polycrystalline with relatively large grains (> 100 nm). The XTEM images indicate the presence of a thin (~ 10 nm) amorphous layer at the TCO/glass interface. The surface of the TCO layer shows considerable roughness, ~ 100 nm, which is consistent with the grain microstructure and the grain sizes. Figure 12A indicates that the grains of the nc-Si are ~ 10 - 30 nm, much smaller than the roughness induced by the grain structure of the TCO layer. Grain collisional behavior related to the texturing of the Asahi TCO (surface roughness induced by the grain structure) is observed as the grains grow away from the TCO surface.

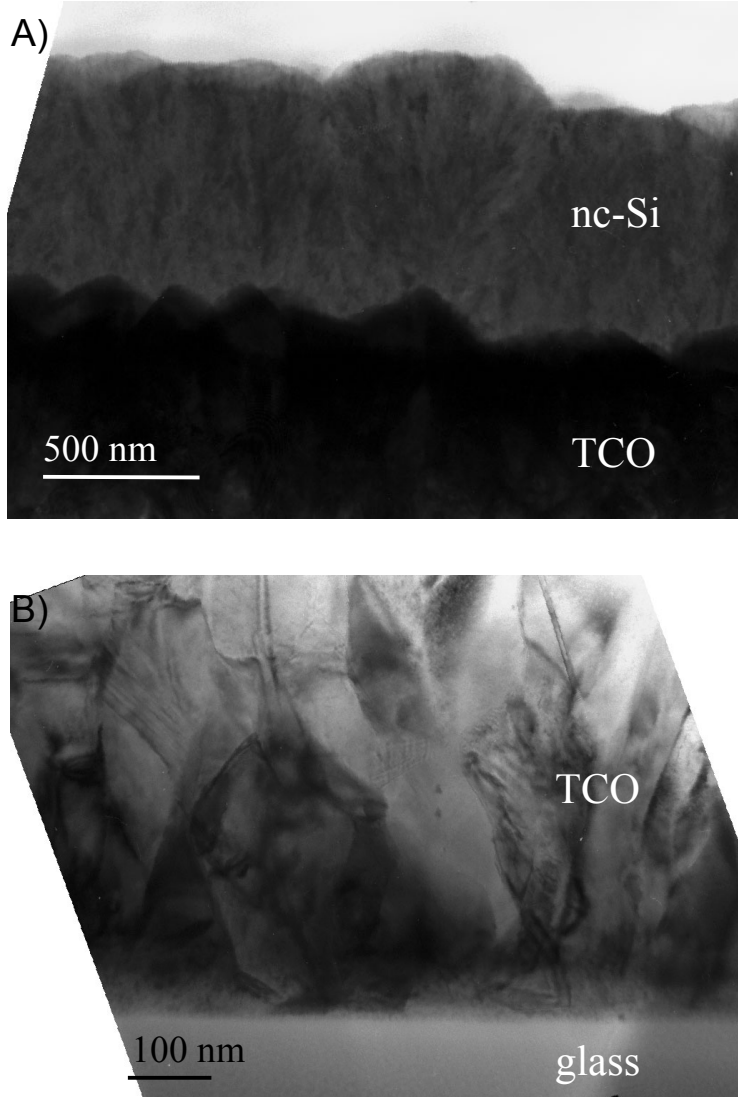


Figure 12. XTEM images of a nanocrystalline Si solar cell on Asahi TCO (Sample 6, Table 3). 12A) Overall microstructure of the device; 12B) microstructure of the TCO layer.

The solar cell device Sample 7 is prepared under the same conditions as Sample 6. In Sample 7 the only difference is the substrate; instead of TCO, textured ZnO was deposited on the glass substrate prior to the nc-Si layer. XTEM images of the overall microstructure of Sample 7 are shown in Figure 13A and 13B.

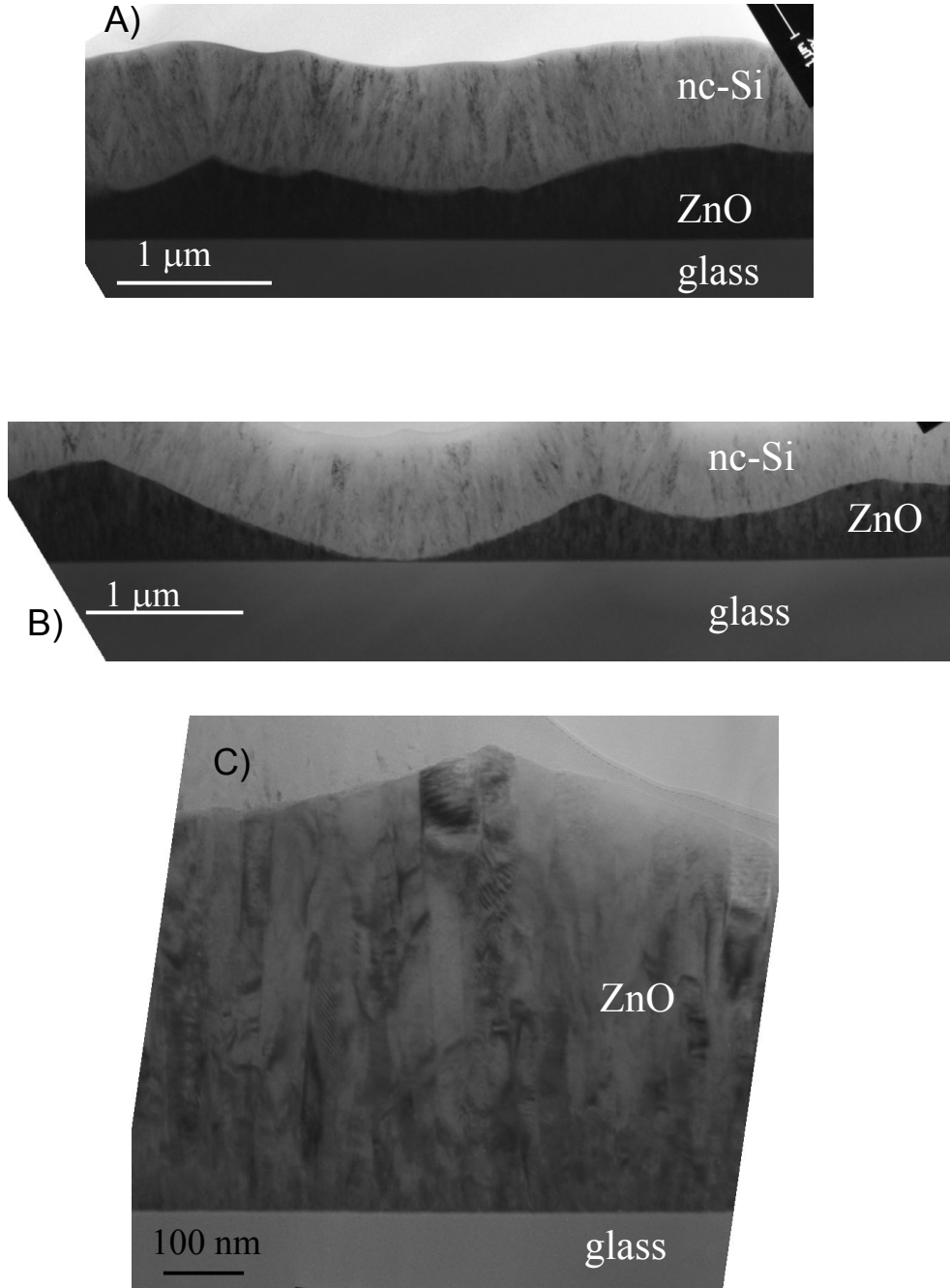


Figure 13. XTEM images of a nanocrystalline Si solar cell on textured ZnO (Sample 7, Table 3). 13A) & 13B) Overall microstructure of the device; 13C) microstructure of the ZnO layer.

It can be seen that the ZnO thickness is not uniform; it varies from 20 nm to more than 1 μm over large lateral distance of \sim several μm . The nc-Si is seen to form a dense layer that follows the variations in the ZnO thickness. The ZnO microstructure can be seen in Figure 13C; it consists of columnar grains with lateral size below 100 nm and length that can reach more than a μm . Small-scale local roughness on the surface of the ZnO layer consistent with its columnar morphology can be distinguished. It is clear that this roughness is not related to the ‘large-scale’ variation in thickness (texture) mentioned above. XTEM images of the nc-Si layer are shown in Figure 14A – C. The images are different in that they show the microstructure of the nc-Si layer depending on the ‘large scale’ texture of the underlying ZnO: growing on a ‘hill’ (Figure 14A and B) or in a ‘trough’ (Figure 14B and C) of ZnO. The nc-Si material is dense with grain sizes of 10-30 nm. These small grains are seen to form columnar-like structures or elements as they grow. The nc-Si columnar-like elements grow perpendicular to the substrate surface that in this case is the ZnO surface. As the ZnO surface is not flat but locally has a slope the nc-Si columnar elements are not vertical, as they probably would have been if the ZnO surface were flat. As a consequence two distinct kinds of behavior can be observed: (i) when the nc-Si grows on a ‘hill’ (Figure 14A) the columnar-like elements grow (lean) away from one another and no collisional behavior is observed; (ii) when nc-Si columnar elements grow out of the adjacent trough of the textured ZnO surface then pronounced collisions between the columnar elements are seen. The collisional behavior is more pronounced in the case when the slope is steeper, for instance in Figure 14B compared to Figure 14C where the variation in the thickness of the ZnO layer is more gradual. When the thickness variation change is more gradual then the columnar elements are almost vertical and the collisional behavior is obviously delayed. In contrast, when the change of the trough in the underlying surface is steep and small (Figure 14B) more pronounced collisions are observed that even lead to microvoid formation along the columnar elements (see right-hand side of Figure 14B).

From the XTEM investigation of Samples 6 & 7 and the comparison of their microstructure, two trends emerge. (i) The nc-Si material microstructure is independent of the microstructure of the underlying substrate - in Sample 6 the grains of the Asahi TCO are larger than 100 nm and in Sample 7 the underlying ZnO has columnar structure with columns with lateral size much smaller than 100 nm. The nc-Si in both cases consists of grains of 10-30 nm that cluster into columnar-like elements. The columnar elements grow perpendicular to the surface of the underlying material. (ii) The ‘large-scale’ texture of the layer on which the nc-Si material is deposited is directly related to

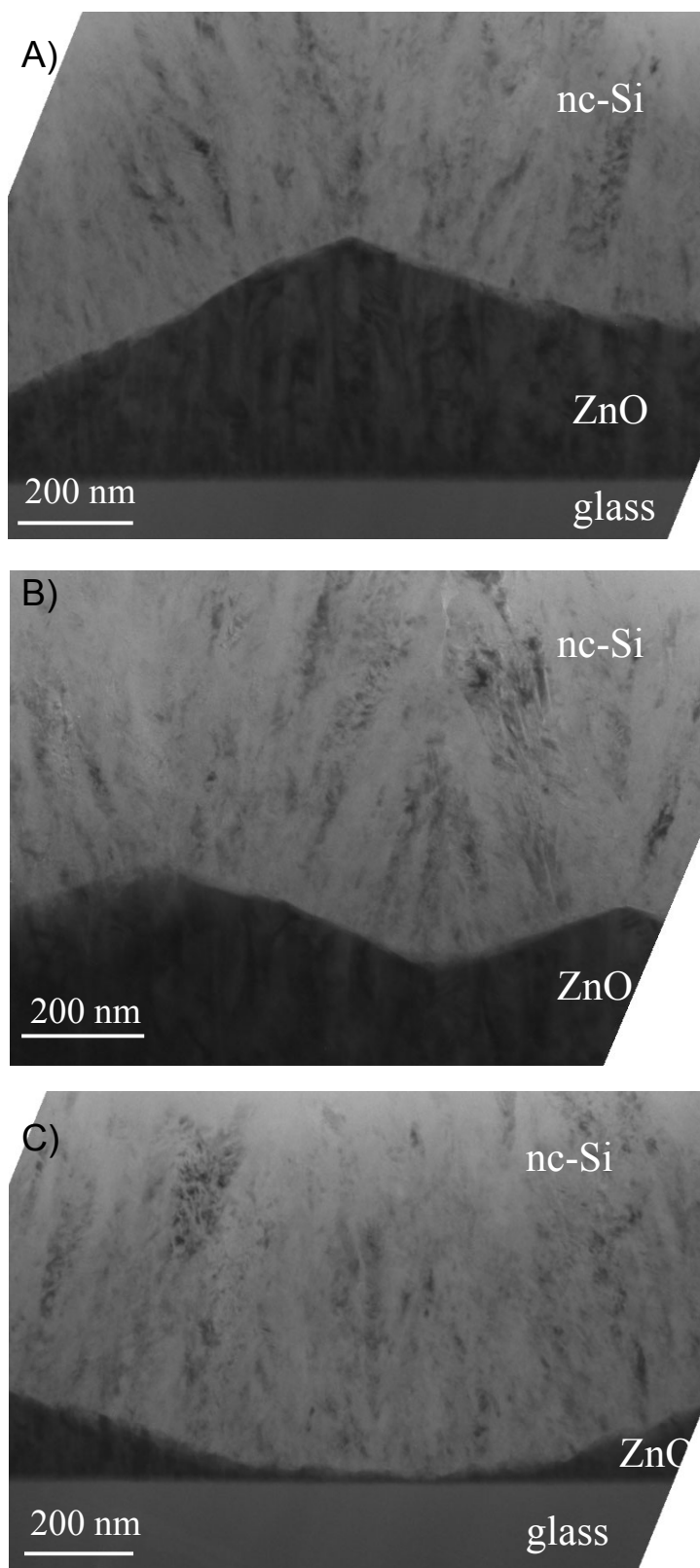


Figure 14. XTEM images of the microstructure of the nanocrystalline Si layer of Sample 7 as a function of the texture of the underlying ZnO layer.

the collisional behavior in the nc-Si layer. In the case of larger roughness changing over smaller lateral distance more collisional behavior is observed together with larger numbers of microvoids (Sample 6). In comparison, Sample 7 demonstrates less collisional behavior that correlates well with its improved device performance, as measured at NREL [see Table 3].

The microstructure of a polycrystalline Si (poly-Si) thin film on Al-coated Corning 7059 glass substrates by HWCVD was investigated [9]. The XTEM images of the microstructure of Sample 8 are shown in Figure 15 A – C. The Al layer thickness is $\sim 1 \mu\text{m}$ and is seen clearly in Figure 15 A and B. The XTEM analysis of the Si material reveals that it consists of large grains and nanocrystalline regions. These two regions can be found either side by side on the Al layer, or as layers with one evolving from the other. This finding is demonstrated in Figure 15: Figure 15A shows one large grain Si ($\sim 1 \mu\text{m}$) on top of the Al layer. Figure 15B shows several large Si grains on the Al layer, but these grains exhibit structural defects such as twins. Figure 15C shows the top surface of the Al layer, a large Si grain of $\sim 300 \text{ nm}$ height and nanocrystalline Si on top of this grain. The finding that micrometer-size grains can be achieved using an in-situ grain enhancement process [9] that did not require any post-deposition treatments such as solid-phase crystallization, laser-annealing or metal-induced crystallization is promising. However, the likely presence of Al-doping of the poly-Si may be problematical for i-layers in cells.

Two microcrystalline Si films (Sample 9 & 10) deposited in the RTSE chamber at NREL were investigated. The microstructure of the two films appeared very similar. XTEM images of Sample 10 are shown in Figure 16A - D. Figure 16A shows the overall structure of this film. It can be seen that the film is nanocrystalline. The interface between the nc-Si film and the crystalline Si interface is hard to see as both samples showed a tendency for delamination that complicated the sample preparation and the consecutive imaging of the film/substrate interface. Figure 16B shows details of the nc-Si film close to the substrate; it can be seen that the growth starts amorphous. The amorphous material appears to be homogeneous and uniform. After a certain thickness (estimated here at $\sim 200 \text{ nm}$) onset of nanocrystalline (cone-like) growth is observed. Immediately with the onset of nc-Si ‘cone-like’ growth microvoids or non-uniform density regions are seen to form in particular where two cones intersect. Figure 16C is a higher-magnification image from the nc-Si material. Figure 16 D shows the microstructure close to the top surface of the nc-Si material. Dense network of microvoids can be seen to propagate to the top surface of this sample.

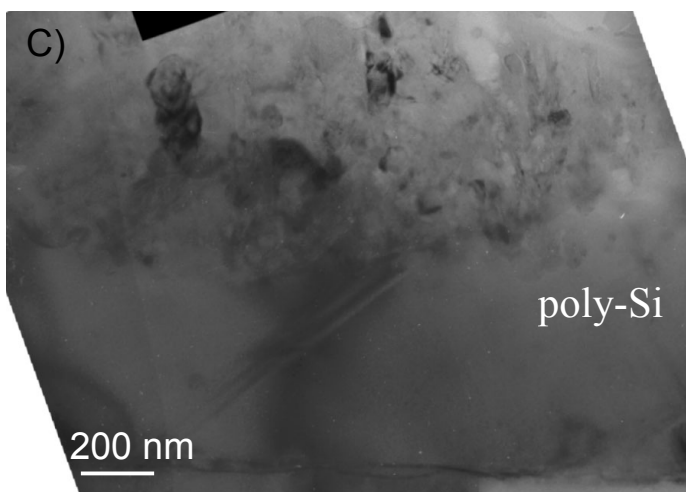
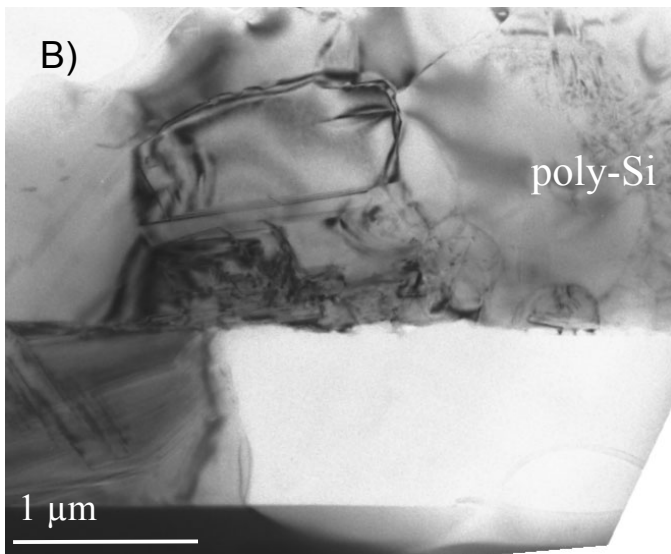
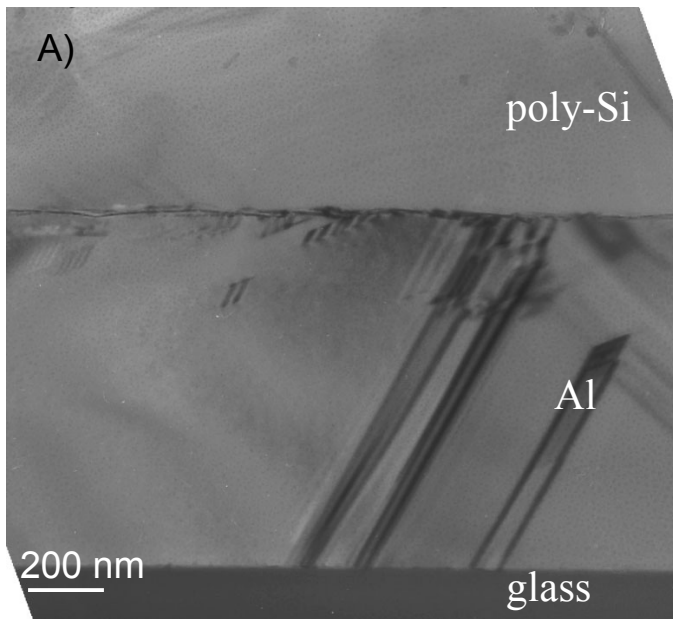


Figure 15. XTEM images of the microstructure of the polycrystalline Si film on Al-coated glass (Sample 8, Table3). 15A) Microstructure of the Al layer deposited on the glass substrate; 15B) overall microstructure of Sample 8 with poly-Si layer showing large Si grains; 15C) details of the poly-Si layer showing a coexistence of large grains and nanocrystalline Si.

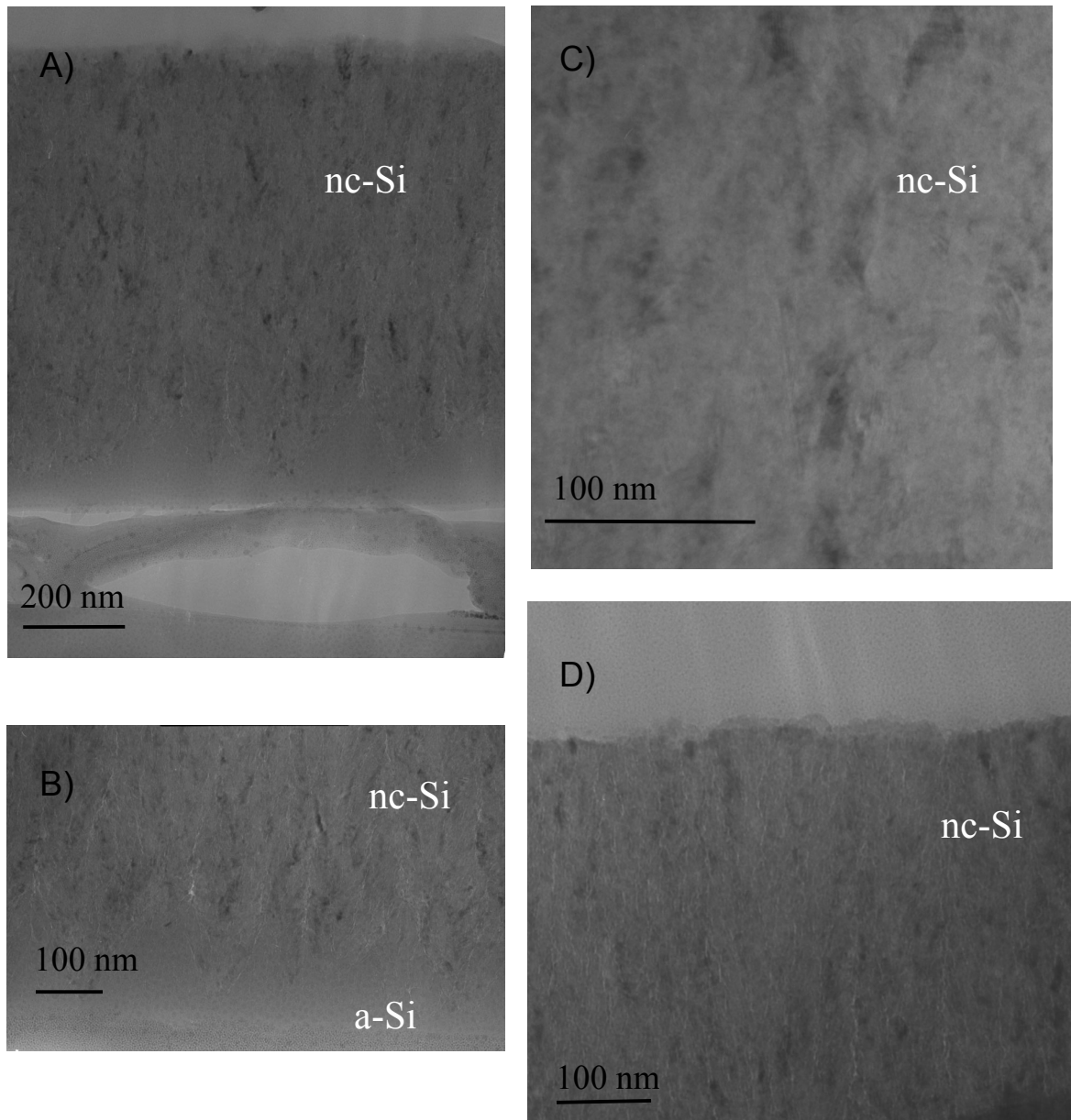


Figure 16 . XTEM images of the microstructure of the microcrystalline Si film (Sample 9 &10, Table3). 16A) Overall microstructure of samples 9 & 10; 16B) microstructure of the area close to the film/substrate interface showing initial formation of amorphous Si and subsequent change to microcrystalline growth; 16C) details of the micro-Si layer; 16D) microstructure of the top part of the Si film, close to the surface.

3.2 Small-Angle Scattering Experiments (Task 2)

3.2.1 SANS Quantitative Interpretation

Experimental SANS results and their detailed interpretation have been published [3,6]. The TEM results presented above support and clarify the interpretations of three of the samples (identified as 1H and 1D in Ref. 3, and HW-H4 in Ref. 6; referred to as Samples 1 and 3, and Sample 2, respectively, in Table 1 above). For sample 1D, the PECVD a-Si:D film, the interpretation of the SANS was complex because of the possibility of several types of microstructures. Based on the clear observation of microvoids/D-rich regions by TEM, we can discard the two-domain model that was based on low-density grain boundary areas surrounding the microcrystals and no microvoids [3].

3.2.2 SAXS Study of BP-Solar a-Si:H Deposition Rate Series

Measurements on a BP-Solar series of a-Si:H films versus dc-PECVD deposition rate have been completed as part of a systematic study of numerous properties by several groups. All IR data from NREL was fitted by software in our lab to extract the microstructure factor R for each sample. Figure 17 shows the SAXS data and Figure 18 shows the IR data, both of which indicate a systematic increase in the heterogeneity with increased deposition rate (the IR 2100 cm^{-1} mode increases relative to the 2000 cm^{-1} mode, i.e., the R-value increases). Table 1 summarizes all the results from SAXS, IR, and flotation density. Different deposition conditions were used for the second 1.0 nm/s sample (A2304-3) and it seems to have reduced heterogeneity based on both the SAXS and R-value. Electronic properties of companion films and cells show a strong correlation with these microstructural results [10].

Table 4. Results from IR, SAXS, and flotation density studies of BP-Solar a-Si:H films. [H] = bonded H content from IR. R = microstructure factor from IR 2000-2100 cm^{-1} stretch modes. Q_N = integrated SAXS intensity from nanostructural features. I_D = diffuse scattering intensity. D_{mp} = most probable sphere diameter. $\langle D \rangle$ = volume-fraction-averaged sphere diameter. ρ_{flot} = flotation density. ρ_H = density based on correlation $\rho_H = 2.291 - 0.0068 [\text{H}]$. f = void fraction based on Q_N , corrected by tilt effect (Q_0/Q_{45}) for only L2137.

Sample	Dep. Rate (nm/s)	[H] (at.%)	R	Q_N (10^{22} eu/cm^3)	I_D (eu)	D_{mp} (nm)	$\langle D \rangle$ (nm)	ρ_{flot} (g/cm ³)	ρ_H (g/cm ³)	f (vol.%)
L2127	0.1	10.4	0.16	3.1	12.5	4	4	2.22	2.22	0.02
L2129	0.3	11.6	0.24	13.4	15	2	6	-	2.21	0.08
L2136	0.5	12.2	0.24	14.3	16	2	6	2.20	2.21	0.08
A2304-1	0.7	16.5	0.50	57	17	1	1.7	2.15	2.18	0.33
A2304-3	1.0	16.3	0.38	46	17	1	1.9	2.17	2.18	0.27
L2137	1.0	16.1	0.60	126*	~ 20	0.8	1.2	2.13	2.18	0.6

* $Q_0/Q_{45} = 1.5$

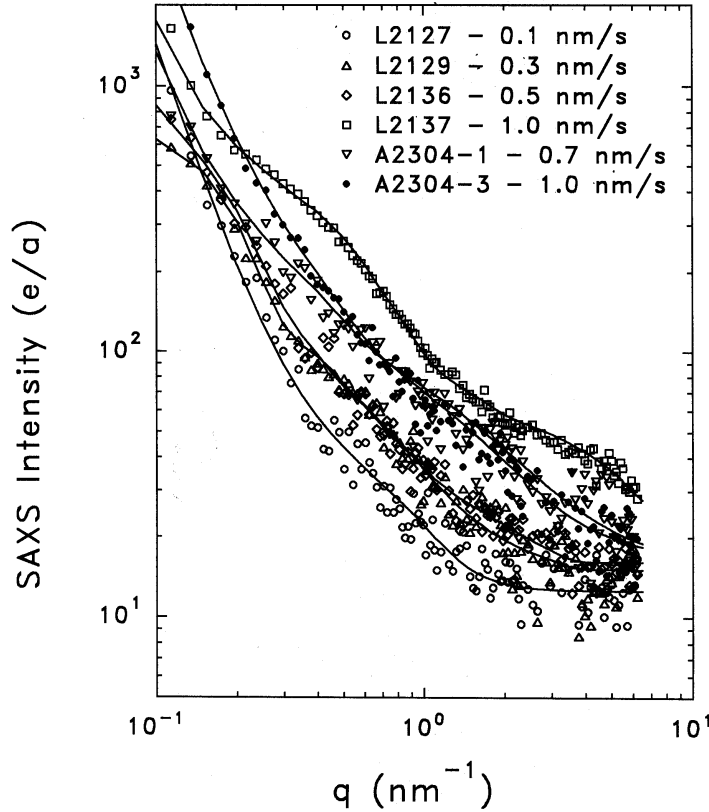


Fig. 17. SAXS data and fits (solid lines) for the six BP-Solar films.

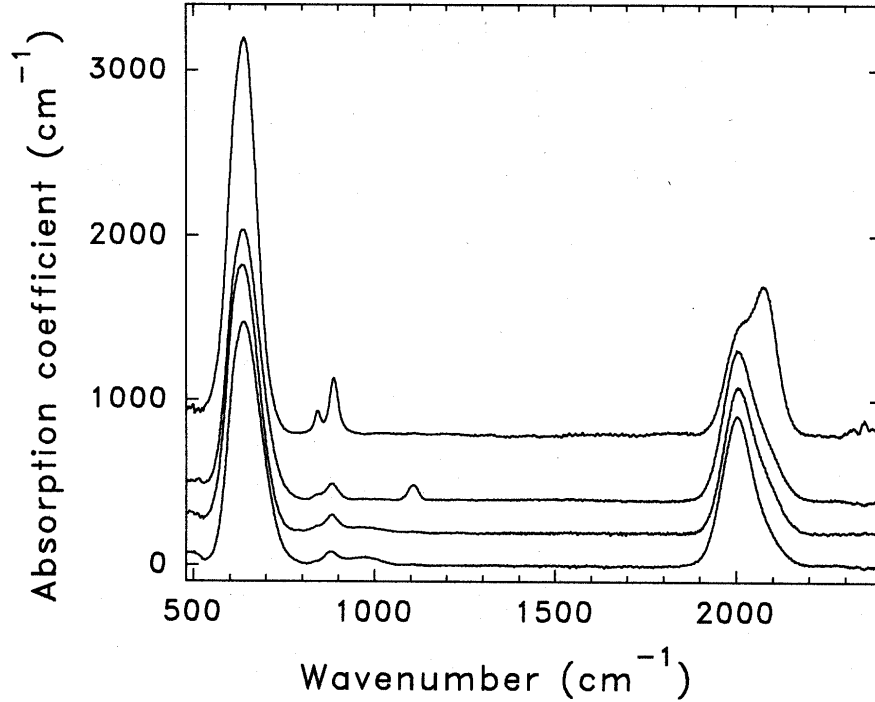


Fig. 18. IR data from four BP-Solar films, L2127 (0.1 nm/s), L2129 (0.3 nm/s), L2136 (0.5 nm/s), and L2137 (1.0 nm/s), from bottom to top, shifted for clarity.

3.2.3 SAXS Study of HWCVD α -SiGe:H Alloys

Three systematic series of alloy films prepared at NREL by HWCVD have been investigated by SAXS and correlated with several other properties measured at NREL. A first series was made with various Ge contents (x) at fixed substrate and filament temperatures. The quality of these films was significantly improved [11] compared to earlier alloys made by the same technique [12], and this was effected by reducing the filament diameter and the substrate temperature compared to the earlier study. Figure 19 shows that the SAXS-determined heterogeneity (Q_N = integrated intensity) increased systematically with x , and was not improved compared to the earlier alloys [13]. One film in that series was made at a lower filament temperature and as indicated in Fig. 19 (sample L828), it showed much reduced SAXS at even a

higher x . This sample also showed an unusually high photoresponse for this x . This led to an optimization study involving filament temperature (T_f) and substrate temperature (T_s) [14]. By lowering both T_f and T_s well below their standard previous levels of 2150°C and 350°C, respectively, significant improvements in opto-electronic properties and microstructures were found. Details of the H contents and bonding as determined by IR, optical gaps, dark and photoconductivities, and the SAXS results are presented in ref. 14. Here we present the strong correlation between the SAXS integrated intensities and the photoconductivities of these two alloy series. Figure 20 shows the SAXS data from the T_f series where one can see the systematic reduction in SAXS as T_f is lowered. Figure 21 compares effects of T_f and T_s on the integrated SAXS intensities (Q) and the corresponding photoconductivities from companion films made under similar conditions. The correlations are clearly indicating that better homogeneity is leading to improved photoconductivity.

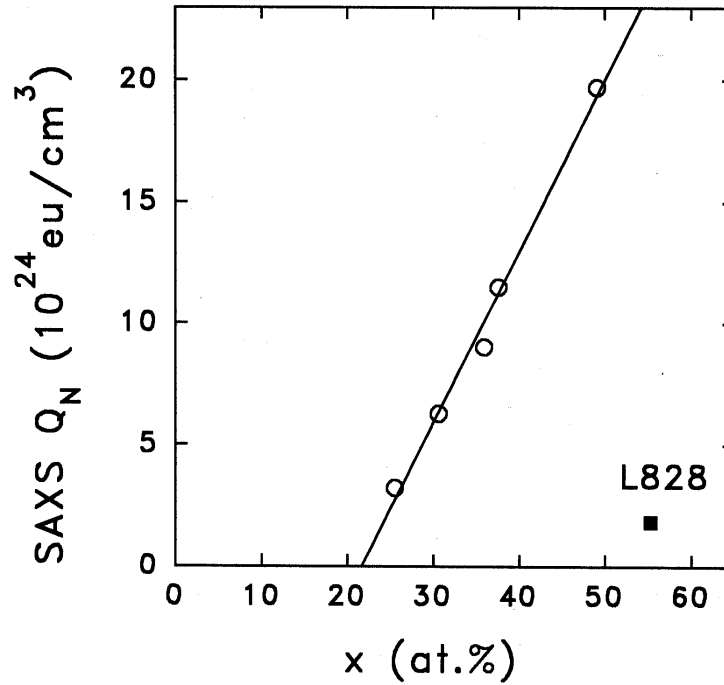


Fig. 19. SAXS integrated intensities from HWCVD a-SiGe:H series of alloys made with reduced filament diameter and reduced substrate temperature. For sample L828 the filament temperature was lowered from 2100°C to 1800°C and the substrate temperature from 250°C to 150°C.

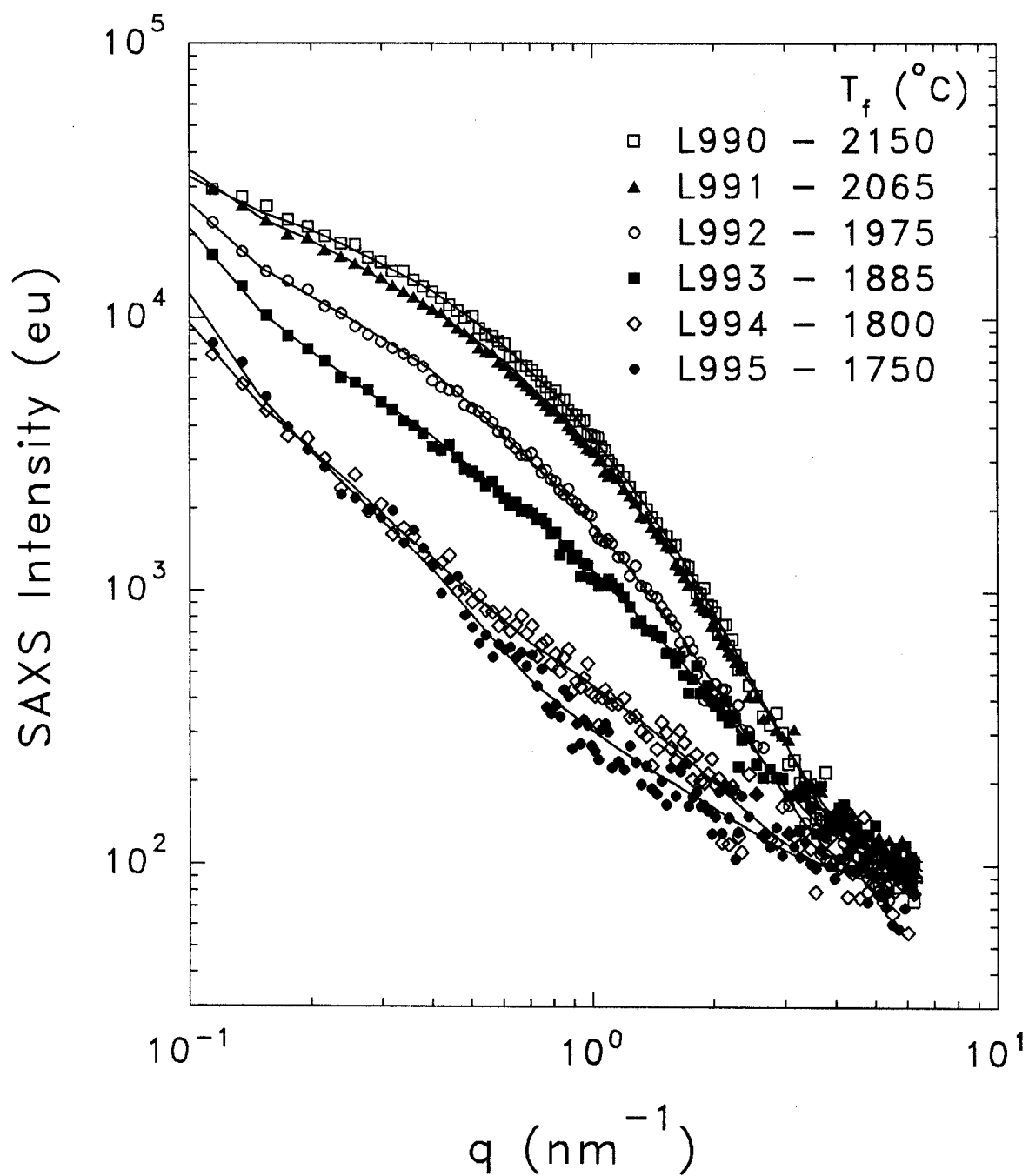


Fig. 20. SAXS data from NREL HWCVD a-SiGe:H alloys made with different filament temperatures at a fixed substrate starting temperature of 180°C .

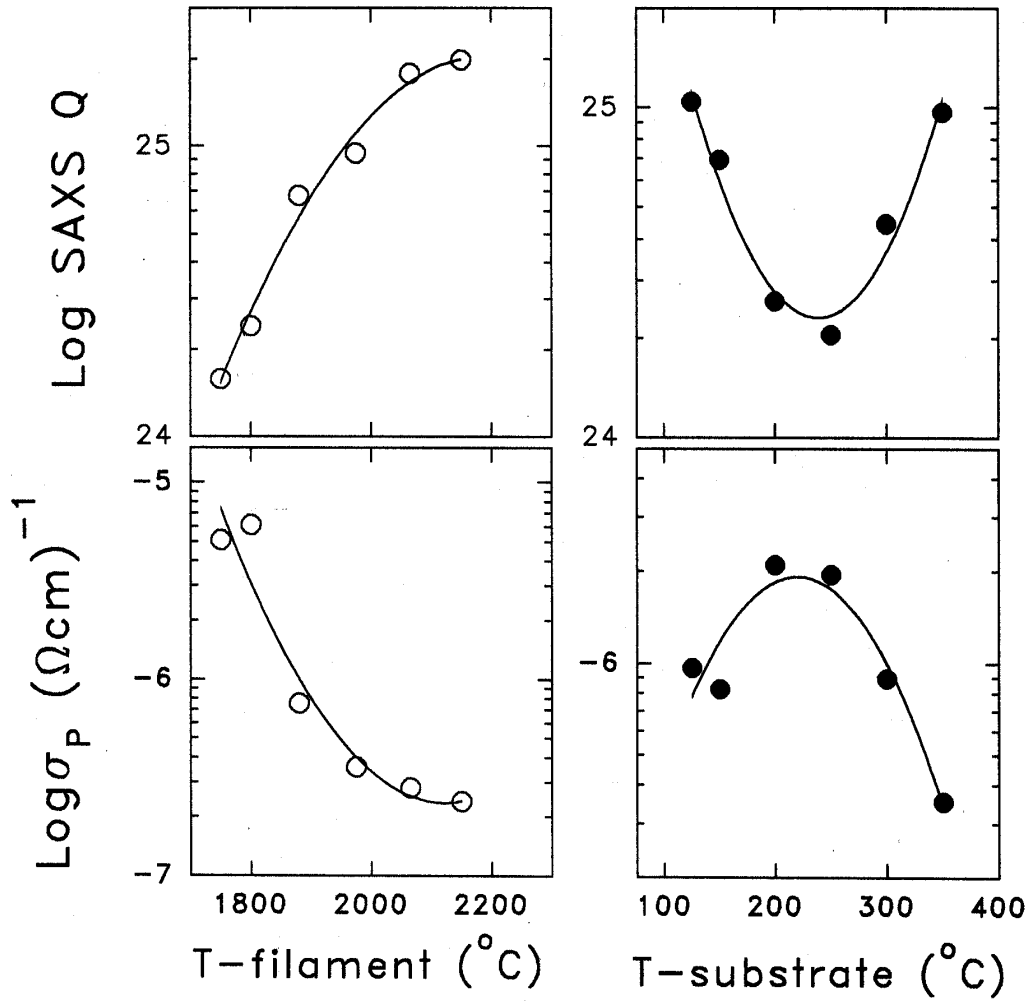


Fig. 21. Correlation of SAXS integrated intensity and photoconductivity for the T_f and T_s series of a-SiGe:H alloys.

3.2.4 SAXS Study of HWCVD a-Si:H Deposited at High Rate with H Dilution

NREL is attempting to improve the microstructure of the ultra-high deposition rate HWCVD material by using hydrogen dilution. Three samples have been prepared for SAXS under conditions listed in Table 5. The 3rd sample (L944) was prepared with conditions nominally identical to the first sample (L942) except the substrate was changed to c-Si since there was evidence of Al-induced crystallization on the SAXS Al-foil substrate. Figure 22 shows the SAXS data from the three films. One can see the following features: (a) the SAXS from L942 and L944 is nearly identical except for a steeper rise at low q for L942, probably due to the slight partial crystallization of L942 (detected

by XRD); (b) the SAXS from L943 is noticeably stronger, perhaps due to the lower substrate temperature, documented earlier as inducing more heterogeneity [1]. Table 6 lists the SAXS quantitative results from the fits shown as the solid lines in Fig. 22.

Table 5. HWCVD preparation conditions for SAXS samples using hydrogen dilution. All were made with a 3-filament configuration.

Sample	H ₂ /SiH ₄	T _s (start) (°C)	T _s (end) (°C)	Dep. Rate (nm/s)	Thickness (μm)
L942	2.3	375	456	10	2.1
L943	1.0	301	390	8	1.7
L944	2.3	375	456	10	2.1

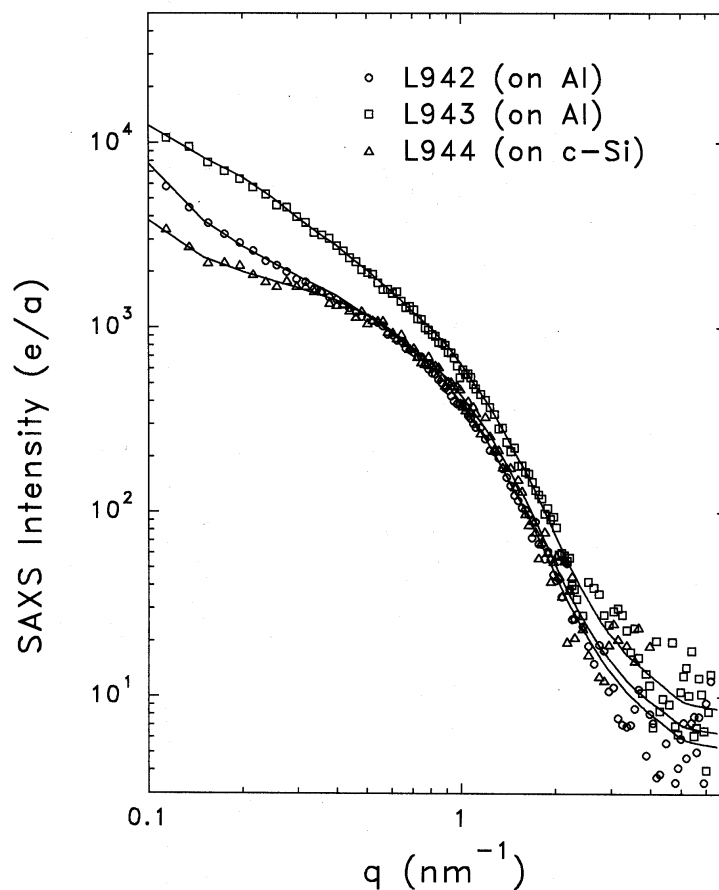


Fig. 22. SAXS data from NREL HWCVD a-Si:H made with H dilution.

Table 6. Quantitative SAXS results from hydrogen diluted HWCVD films. Q_N is the integrated SAXS intensity, A the Porod slope, I_{diff} the diffuse intensity, and $\langle D \rangle$ the average sphere diameter from the distribution fit.

Sample	Q_N (10^{24} eu/cm ³)	A (eu/nm ³)	I_{diff} (eu)	$\langle D \rangle$ (nm)
L942	1.74	5.5	5	4.8
L943	3.19	4.7	8	5.8
L944	1.84	2.0	6	4.4

The Q_N 's can be compared to the earlier results for non-hydrogen-diluted films [5] to indicate that the microstructure has not been improved significantly. The sizes of the scattering features are also similar to those from the earlier films [5]. The relatively low values of I_{diff} are consistent with the relatively low bonded H contents (3.8 at.% and 7.6 at.% from duplicate runs of L942 and L943). The lack of improvement in microstructure is correlated with a lack of improvement in the photoresponse found to date with such hydrogen-diluted material.

3.2.5 SAXS Study of USSC Microcrystalline Solar Cell Materials

Three microcrystalline-Si:H films were provided by USSC. Three different deposition methods with different deposition rates were used as summarized in Table 5, which includes some H content data from SIMS depth profiles on similarly deposited films. The H content was high at the beginning of deposition and decreases with thickness, probably related to microcrystallinity evolution with thickness. Both SAXS and flotation density measurements were completed. Tilting SAXS was done to look for oriented microstructure. Also, before folding the films for SAXS, XRD patterns were acquired.

Table 7. Preparation and composition of USSC μ c-Si films for SAXS. Hydrogen contents from SIMS given in at.%.

Sample I.D.	Method	Rate	[H] -low	[H]-high	[H]-average
Line14110	RF-PECVD	Low (~ 0.1 nm/s)	6.8	5.6	6.2
RF11817	MVHF-PECVD	High (~ 0.3 -1 nm/s)	7.2	4.4	5.8
BMW7427	μ wave-PECVD	Very high (~ 2 -3 nm/s)	9.6	8.0	8.8

Figure 23 shows the SAXS data from the three films. The intensities are high from all three and show slightly different shapes, indicating different size distributions of scattering objects.

Distributions of spheres were used to fit the data and this yields the solid lines through each data set shown in Fig. 23. Each sample was tilted at 45 degrees relative to the x-ray beam and the resulting SAXS data show that all three have some oriented microstructure but it is more significant in the RF and MVHF samples. Quantitative results are summarized in Table 8.

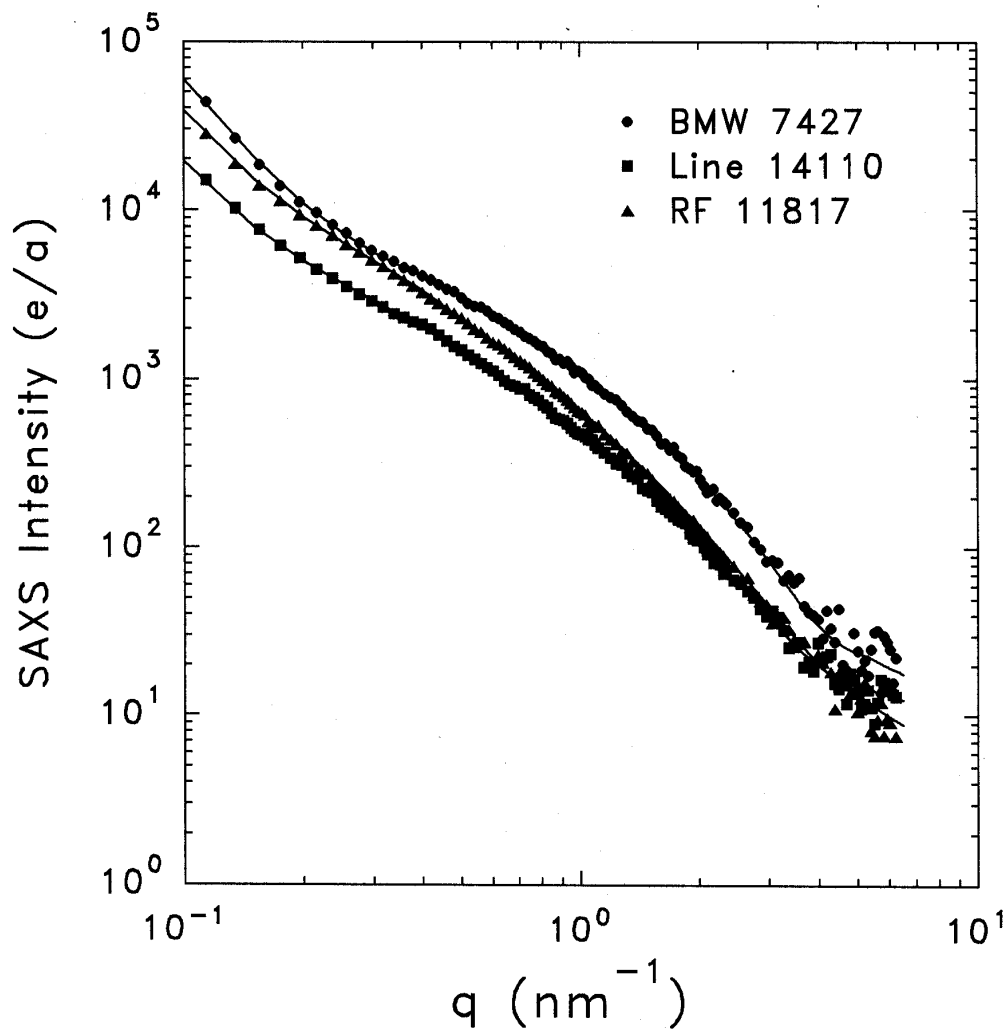


Fig. 23. SAXS data from three USSC microcrystalline-Si:H films and fits (solid lines) of sphere distributions.

Table 8. SAXS and flotation density results from microcrystalline films of USSC.

Sample	t (μm)	Q_T (10^{24} eu/cm^3)	A_p (eu/nm^3)	I_{diff} (eu)	$\langle D \rangle$ (nm)	Q_0/Q_{45}	f_{max} (vol.%)	ρ_{flot} (g/cm^3)
BMW7427	0.9	7.54	55	12	3.1	1.7	3.1	2.227
RF11817	1.8	4.89	33	7	4.1	3.2	1.2	2.250
LINE14110	1.2	3.19	16	10	3.8	3.7	0.7	2.235

t = thickness based on x-ray absorption (relative values confirmed by XRD pattern intensities);

Q_T = total integrated SAXS intensity;

A_p = Porod slope at low q;

I_{diff} = diffuse (angle-independent scattering intensity);

$\langle D \rangle$ = average sphere diameter (volume fraction average) [or small cross-section of ellipsoids if oriented parallel to growth direction];

Q_0/Q_{45} = ratio of total integrated intensities with sample in non-tilted and 45° -tilted orientations relative to x-ray beam;

f_{max} = maximum void fraction based on correction for ellipsoidal objects oriented parallel to growth direction and assuming all of QT due to microvoids;

ρ_{flot} = flotation density of film removed from Al-foil substrate.

The XRD patterns are shown in Fig. 24. The strong peaks near 38° and $44\text{--}45^\circ$ are due to the Al-foil substrate and a stainless-steel mounting support. One can see the systematic increase in relative intensity of the (220) peak near 47° as the deposition rate decreases from BMW7427 to RF11817 to LINE14110. Similarly, the line widths decrease indicating larger grain sizes. Analysis of the relative integrated intensities and peak widths yields the results listed in Table 9 for the (111), (220), and (311) peaks.

Table 9. XRD results from USSC $\mu\text{c-Si}$ films. Random orientation of crystallites leads to $I(111):I(220):I(311) = 1.00:0.60:0.35$. $L(hkl)$ = grain size from Scherrer equation. I_s/I_{111} = relative intensity of shoulder peak at 27° .

Sample	I_{220}/I_{111}	I_{311}/I_{111}	I_s/I_{111}	L(111) (nm)	L(220) (nm)	L(311) (nm)
BMW7427	0.28	0.21	0.12	6.0	6.1	5.4
RF11817	0.83	0.41	0.10	8.1	10.4	7.7
LINE14110	1.64	0.21	0.35	8.6	25.3	13.2

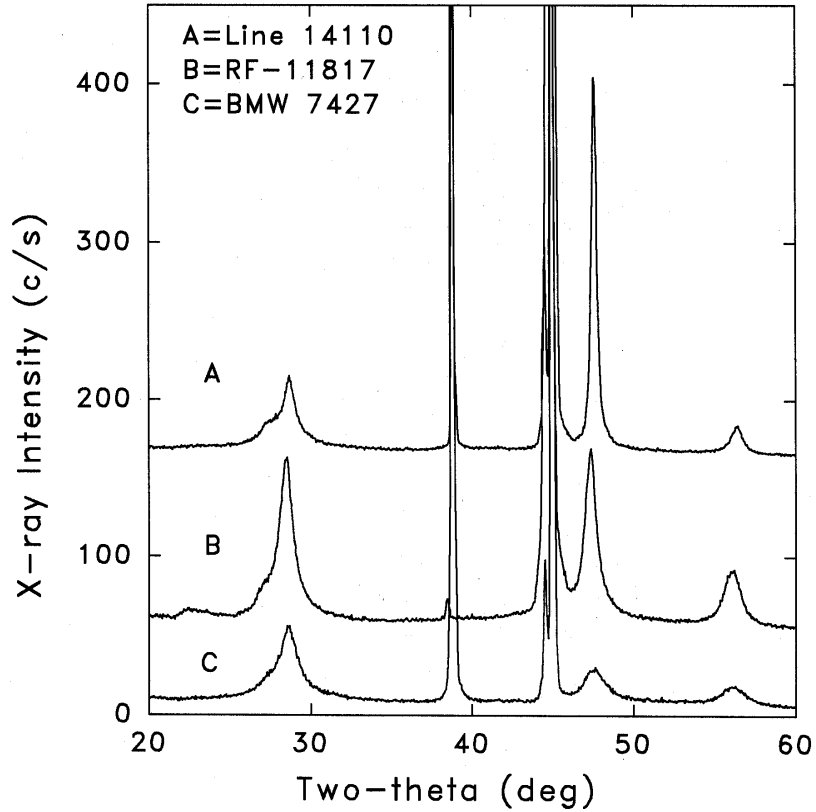


Fig. 24. XRD patterns from three USSC microcrystalline-Si:H films.

Observations/conclusions:

- 1) SAXS intensities are quite strong, typical of $\mu\text{c-Si:H}$ films [1] and Q_T (Table 8) increases systematically with deposition rate implying more heterogeneity with increasing rate.
- 2) Flotation densities are quite high (similar to void-free a-Si:H). Based on our correlation of mass density and [H], $d = 2.291 - 0.0068[\text{H}]$ [1], and the average [H] values in Table 7, the following densities are predicted: Line14110 – 2.249 g/cm³, RF11817 – 2.252 g/cm³, BMW7427 – 2.231 g/cm³. These are only slightly higher than the measured flotation densities. This implies that void fractions are likely significantly less than the f_{max} values in Table 8 and that other heterogeneity contributes to the SAXS signals.
- 3) Lower diffuse intensity (I_{diff} , Table 8) for RF11817 implies this sample has the lowest H content, consistent with the [H] in Table 7 and with the highest flotation density.

- 4) Anisotropic SAXS (Q_0/Q_{45} , Table 8) is strongest for lowest deposition (LINE14110) rate implying that the microstructure is most highly oriented in this film. This result seems to correlate with the XRD results that the (220) texture (I_{220}/I_{111} , Table 9) is strongest for this same film.
- 5) The grain sizes (parallel to growth direction) clearly increase with decreasing deposition rate, particularly the (220)-oriented grains (Table 9). The estimate sizes, $L(hkl)$, are clearly larger than the values of $\langle D \rangle$ from SAXS (Table 8). However, we must keep in mind that SAXS is measuring *lateral* sizes of features, while XRD via the Scherrer analysis is measuring *vertical* sizes. Further analysis (or direct TEM evidence) is needed to unequivocally attribute the SAXS to microvoids.

3.2.6 SAXS Study of KAIST Photo-CVD a-Si:H Films

At the request of a group in the Department of Electrical Engineering and Computer Science of the Korea Advanced Institute of Science and Technology (KAIST), we have analyzed a series of a-Si:H films prepared by photo-CVD [15]. The focus is on the transition from protocrystalline to the mixed amorphous/microcrystalline regime. Table 10 summarizes the samples and data provided by KAIST. Several of these numbers were estimated from figures supplied in powerpoint files. AFM-Lat refers to the average lateral dimension of the surface features, based on the line scans provided, and are only rough estimates.

Table 10. Summary of properties of KAIST films provided. All were prepared by a photo-CVD method, with $T_s = 250^\circ\text{C}$, $P = 0.24$ Torr.

Sample ($R=\text{H}_2/\text{SiH}_4$)	Thickness (μm)	C_H (at.%)	IR_{micro}	Raman ($\mu\text{c-fraction}$)	AFM-rms (nm)	AFM- Lat (μm)
R=0.0	1.0	9.4	0.06	0	1.4	~ 0.1
R=0.5	0.95	10.6	0.05	0	1.2	~ 0.1
R=1.0	1.0	13.3	0.08	0	1.3	~ 0.1
R=1.5	1.0	14.7	0.12	0	8	~ 0.5
R=2.0	1.1	10.5	0.19	0	20	~ 0.5
R=3.0	0.83	4.6	0.33	NA	17	~ 0.2

XRD was used to check for microcrystallinity. Figure 25 shows the diffraction patterns for R=1.5, 2, and 3 samples. There is no evidence of the c-Si (111), (220), or (311) peaks for R=1.5 or R=2. However, the R=3 film is strongly microcrystalline (μc) as can be seen.

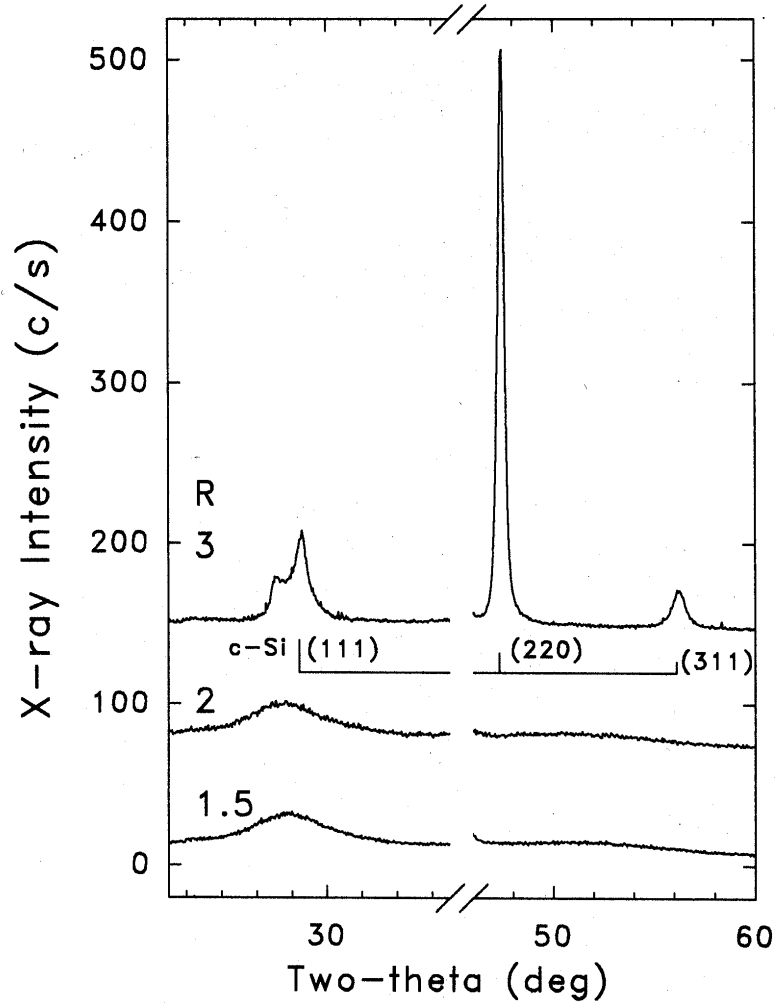


Fig. 25. XRD patterns from KAIST films with increasing R. The angular range from 37° to 46° has been omitted due to strong Al-foil substrate peaks in this range.

From analysis of the pattern by computer fitting, the following results are found for the R = 3 film:

- The μc -Si fraction is $\geq 87\%$ (XRD not very sensitive at such high fractions);
- Relative integrated intensities: $I_{220}/I_{111} = 2.43$; $I_{311}/I_{111} = 0.30$ (compare to randomly-oriented grains: $I_{220}/I_{111} = 0.60$ and $I_{311}/I_{111} = 0.35$). Thus, the film has a strong preferred (220) texture, i.e. grains with a preferred orientation of (220) planes parallel to film surface;

- c) The grain sizes as estimated from the Scherrer equation are: $L(111) = 9 \text{ nm}$; $L(220) = 25 \text{ nm}$; $L(311) = 12 \text{ nm}$. These values represent the grain size in the growth direction and show that the size of the (220)-oriented grains are clearly larger;
- d) There is a clear shoulder on the low-angle side of the (111) peak at 27.1° , which is often seen in $\mu\text{c-Si}$ films [1].

The SAXS data are shown for all samples in Figure 26. There are several features of interest:

- a) Only the $R = 3$ film shows a strong signal indicating a rather large amount of microvoids or other heterogeneity;
- b) The other films all show very weak SAXS at larger q as indicated by the rather large scatter in the data in this range;
- c) All the data flatten out to approximate constant values at high q and this is due to diffuse scattering, I_{diff} , from the atomic-scale fluctuations. I_{diff} tends to increase with the bonded H content;
- d) As q decreases toward the lowest values, the SAXS intensity increases logarithmically to different values and this is likely related to different surface roughness as will be discussed more below.

Figures 27-29 show three of the samples individually so one can see more clearly each set of data and the fits. Figures 27 and 28 include calculated curves corresponding to 0.1 vol.% of microvoids with sizes of 2 nm and 4 nm so one can see that this amount could easily be detected. In Fig. 29, we have included a measurement with the film tilted at 45° relative to the x-ray beam to search for oriented microstructure. One can see the intensity has become smaller upon tilting and this indicates elongated scattering features aligned along the growth direction. Also shown in the inset of Fig. 29 is the size distribution of scattering objects (sphere diameters or the small dimension diameters of ellipsoids) used in the fitting procedure.

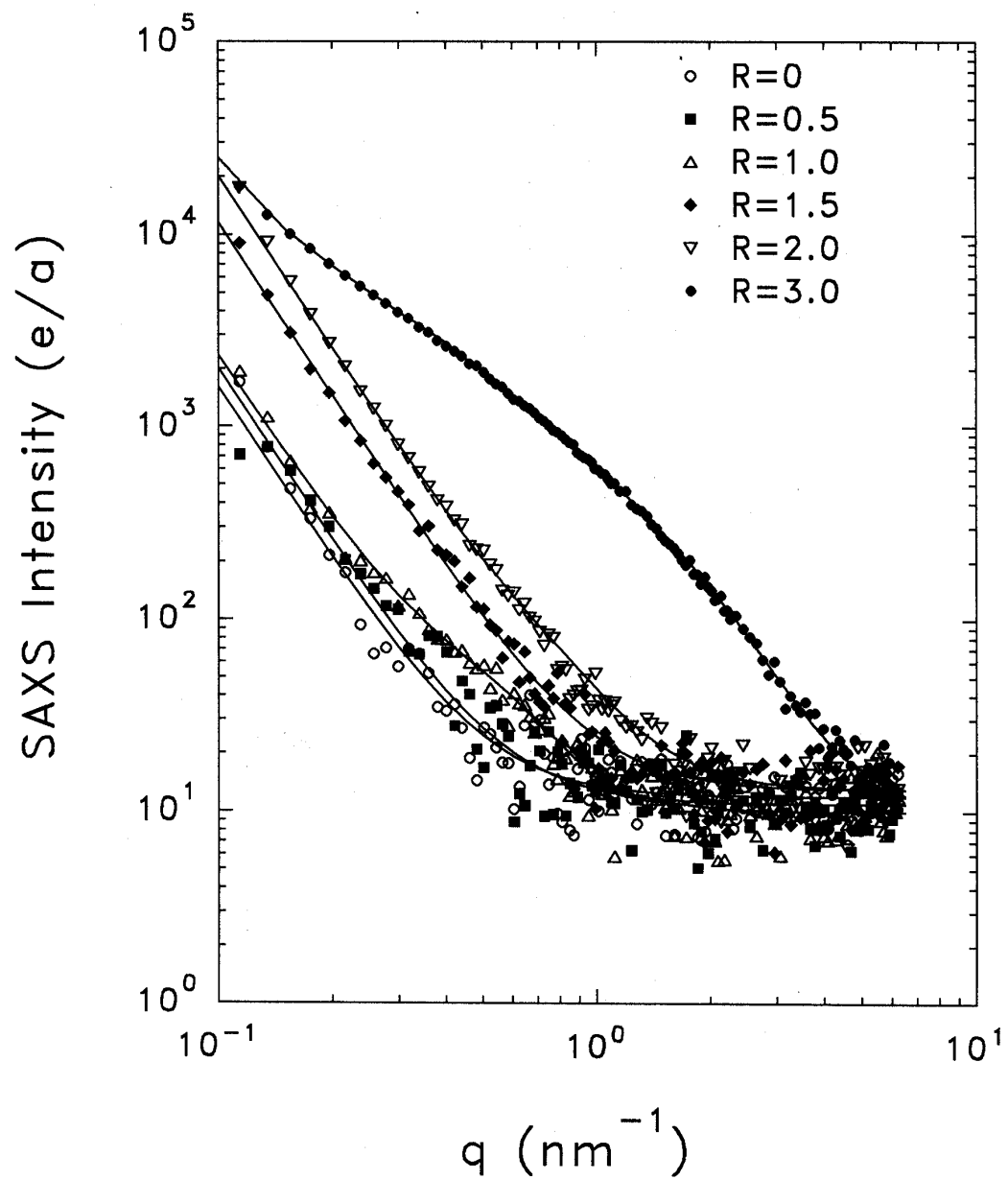


Fig. 26. SAXS data from all KAIST films. Solid lines are fits based on a distribution of spheres, a Porod contribution, and a diffuse scattering contribution.

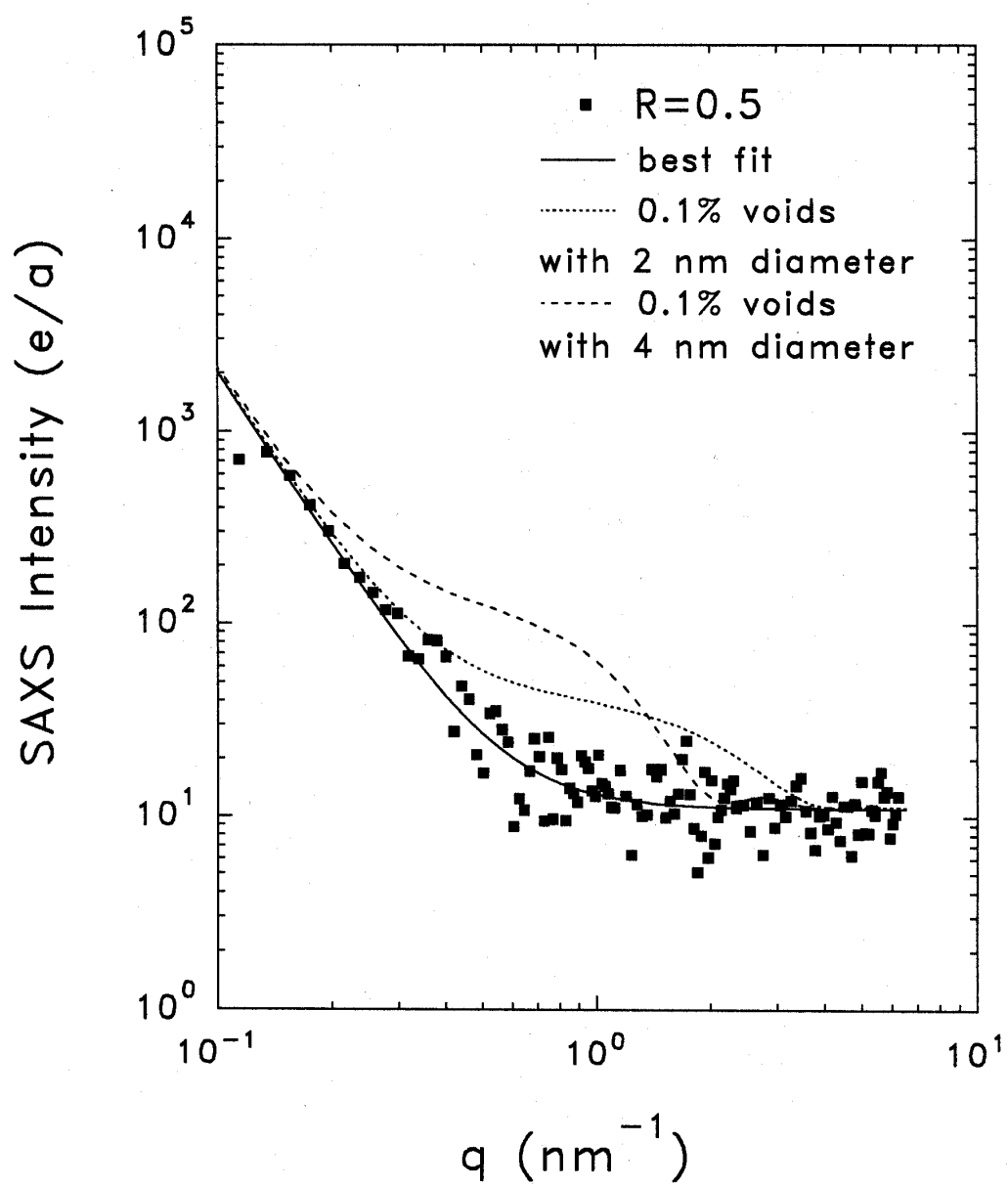


Fig. 27. SAXS $R=0.5$ data, fit to data, and model calculations for spherical voids.

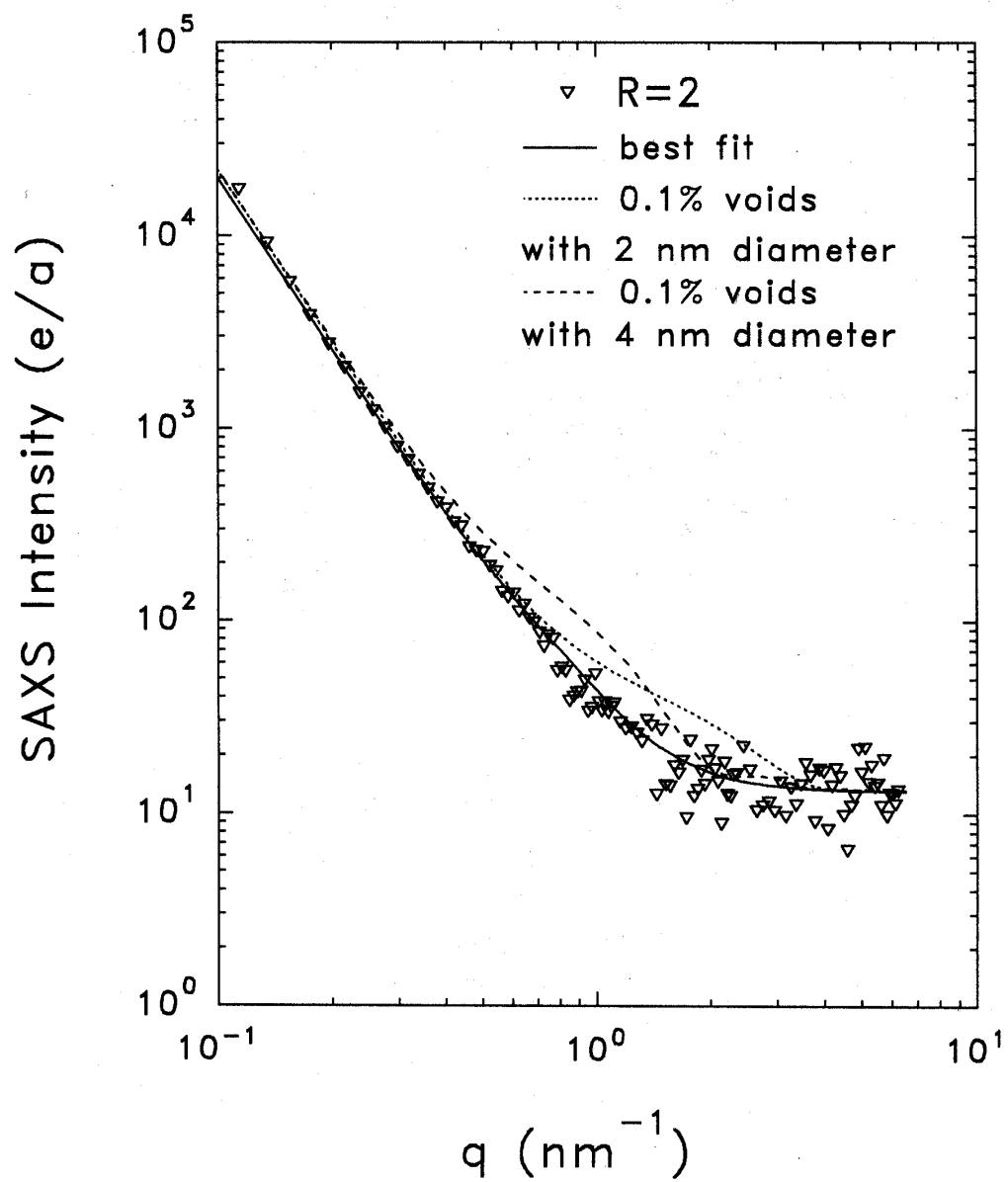


Fig. 28. SAXS $R=2.0$ data, fit to data, and model calculations for spherical voids.

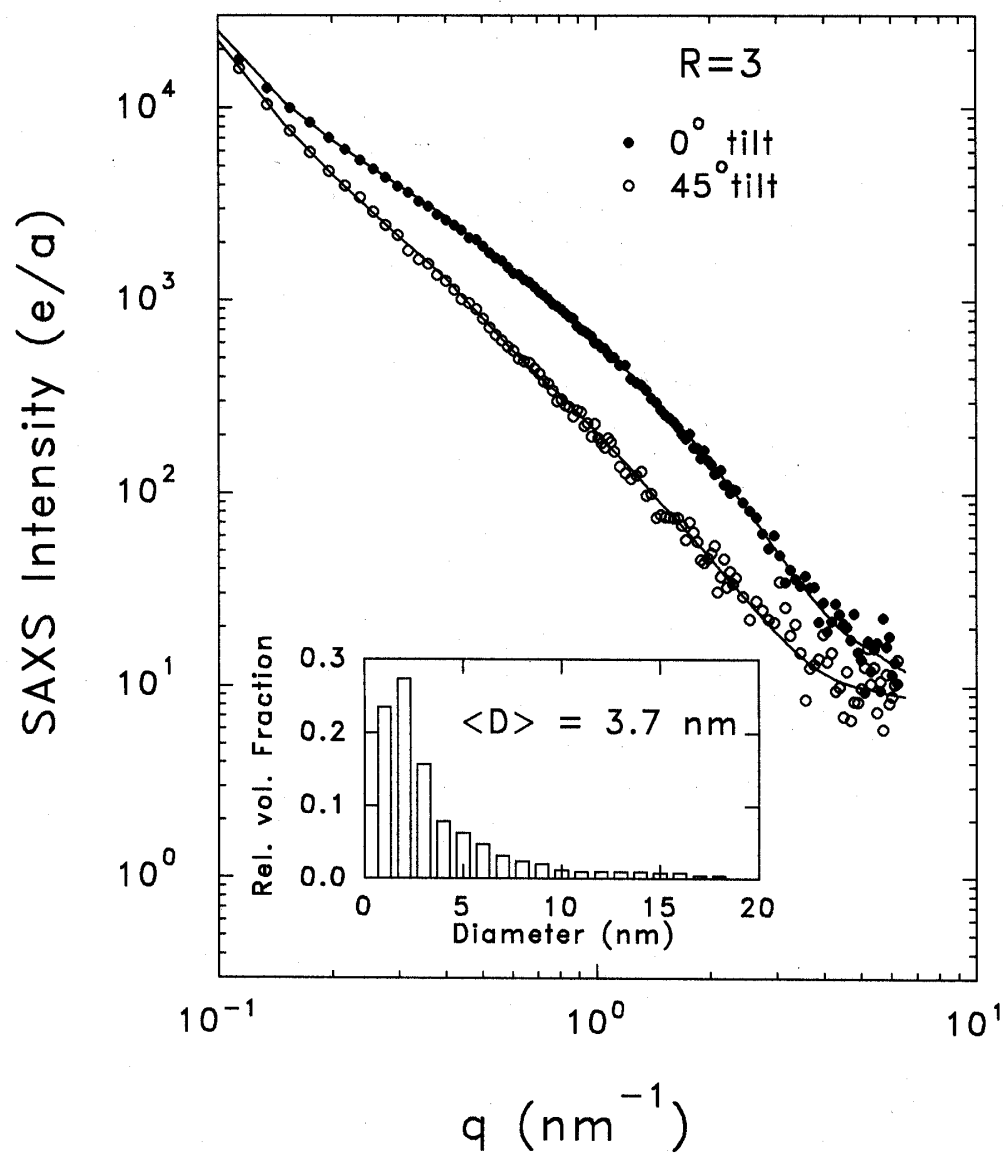


Fig. 29. SAXS R=3.0 data in non-tilted and tilted orientations, fits to data, and size distribution of spheres (inset) for fit to non-tilted data (solid line).

The quantitative results from fitting the SAXS data and also the measured flotation densities are listed in Table 11. The symbols used are described below the table.

Table 11. Quantitative SAXS results and flotation densities for KAIST films.

Sample	Q_T (10^{22} eu/cm 3)	Q_N (10^{22} eu/cm 3)	A_p (eu/nm 3)	I_{diff} (eu)	$\langle D \rangle$ (nm)	F_v (vol.%)	ρ_{flot} (g/cm 3)	ρ_H (g/cm 3)
R=0.0	5.6	≤ 2	1.8	11	-	≤ 0.01	2.228	2.23
R=0.5	6.2	≤ 2	2.0	11	-	≤ 0.01	2.223	2.22
R=1.0	9.5	2.3	2.3	10	7	0.014	2.198	2.20
R=1.5	39	≤ 4	11.5	13	-	≤ 0.02	2.202	2.19
R=2.0	69	≤ 4	22	13	-	≤ 0.02	NM	2.22
R=3.0	434	372	20	8	3.7	0.94	2.236	2.26
R=3.0 (45° tilt)	180	118	20	8	5.9	*	2.236	2.26

Q_T is the total integrated SAXS intensity over the experimental scan range.

Q_N is the nanostructural integrated SAXS intensity based on fits of spherical features in the 1 to 20 nm size range.

A_p is the Porod slope based on fit of A_p/q^3 in the low q range. This is due to features > 20 nm in size.

I_{diff} is the angle-independent diffuse scattering.

$\langle D \rangle$ is the volume-fraction-weighted average diameter of the spheres used to fit the nanostructural contribution to the SAXS. It would also represent the average small diameter of ellipsoids aligned with the growth direction.

F_v is the microvoid fraction based on the Q_N contribution, assuming all of Q_N is due to voids. Thus it represents the maximum possible void fraction based on Q_N .

* The ratio of $Q_N(0^\circ)/Q_N(45^\circ) = 3.15$ was used to estimate a correction to the void fraction of the R=3 sample based on an ellipsoidal model. This ratio and model also implies that the average long dimension of the ellipsoids is a factor of 5 larger than the average 3.7 nm small dimension ($\langle D \rangle$ in table).

ρ_{flot} is the measured flotation density accurate to ± 0.010 g/cm 3 . NM implies that this density of this sample was not measurable due to the films breaking up into such fine particles that they could not be measured in the flotation fluid.

ρ_H is a calculated mass density based on the bonded H contents from IR (listed below) and a correlation established in our lab given by $\rho_H = 2.291 - 0.0068C_H$ [1]. This correlation was found for samples that had undetectable void fractions by SAXS. Thus a lower value for ρ_{flot} compared ρ_H is clear evidence for voids.

Observations/conclusions:

- 1) The results appear quite systematic in general, with good correlations among some of the parameters. The SAXS-determined void fractions are all very small except for the R=3 sample,

which is strongly microcrystalline. Sample R = 1 seems to have a small Q_N signal (however, only slightly larger than the detection limit), but the size of 7 nm seems too large for typical microvoids. It may be due to surface roughness features.

- 2) Note that the average size of $\langle D \rangle = 3.7$ nm is much smaller than the grain sizes estimated from the XRD data (9 to 25 nm) so the SAXS is not likely related to the grain sizes but rather to voids and low-density regions between the grains.
- 3) Although the flotation density method is not very sensitive for detecting small amounts of voids, the flotation density agrees well (within the error) with the calculated density based on C_H , with the exception of the R = 3 sample. This is consistent with the SAXS which indicates very small void fractions in all samples but R=3. The difference between ρ_{flot} and ρ_H for this sample (0.024 ± 0.010 g/cm³) is consistent with the SAXS-estimated void fraction of 0.94%.
- 4) The SAXS does show a systematic increase in the Porod slope, A_P , and this seems to be correlated with the surface roughness rms values. In fact, the rms values (Table 10) increase nearly the same relative amount as the A_P values (Table 11). The lateral size of the surface features (Table 3) implies that the SAXS due to these will be mostly at very small q values below the experimental q range and only the Porod range (where $I = A_P/q^3$) of their scattering will be visible in the experimental q range.
- 5) The diffuse intensity, I_{diff} , is quite uncertain due to the scatter (about ± 2 eu) but seems to correlate with the bonded H content as expected.
- 6) The photo-CVD films with R = 0 to 2.0 are very homogeneous and similar in structural quality with the best films we have analyzed that were grown by PECVD and HWCVD. The R=3 film shows strong non-homogeneity, similar to all other microcrystalline films we have studied recently. It appears that the transition region, just *above* the onset of microcrystallinity, will be *difficult* to study since these samples studied so far have either 0 % crystallinity (according to XRD and Raman) or >87 % crystallinity (according to XRD).

3.2.7 SAXS Study of DTU Microcrystalline Films

We have analyzed two sets of films (4 each) supplied by Delft Technical University (DTU) that were prepared by expanding-thermal-plasma CVD (ETP-CVD) [16]. The goal is to increase the deposition rate for $\mu\text{c-Si:H}$ solar cell material. The SiH_4 flow is varied to cover the transition from amorphous to microcrystalline material. The substrate temperature was fixed at 300°C. For the first

film series the SiH₄ injection ring was positioned close to the plasma source exit at 365 mm above the substrate and for the second series it was placed much closer to the substrate at 55 mm. The deposition rates ranged from 0.91 to 1.52 nm/s.

The eight films were measured by XRD before folding into 8 layers for SAXS. Figure 30 shows the XRD patterns, which are organized in terms of increasing crystallinity from bottom to top. The strong lines near $2\theta = 38^\circ$ and 44° are due to the Al-foil substrate. Using our procedure for determining the $\mu\text{c-Si}$ fraction [17], the values found (F) are listed in Table 12. The fitted linewidths of the (111), (220), and (311) $\mu\text{c-Si}$ peaks are also listed in the table (W) and were used to estimate grain sizes (L) from the Scherrer formula as listed in the table. Other features in the XRD data include evidence of a broad peak near 23° for sample #3, perhaps indicating some Si-oxide formation, and a shoulder on the low side of the (111) peak at 27.1° for #3, often seen by us and others for more fully microcrystalline films, but not yet well understood [1].

Table 12a. XRD results from first DTU series (365 mm position)

Sample	F (%)	W(111) (2θ)	L(111) (nm)	W(220) (2θ)	L(220) (nm)	W(311) (2θ)	L(311) (nm)
#2	0	-	-	-	-	-	-
#1	12	1.26 ^a	6.6	1.26 ^a	6.9	1.26 ^a	7.2
#4	50	0.82	10.1	1.58	5.5	1.30	7.0
#3	58	0.50	17.2	1.36	6.4	1.30	7.0

a. Fixed to be same in fitting due to weak peaks

Table 12b. XRD results from second series (55 mm position)

Sample	F (%)	W(111) (2θ)	L(111) (nm)	W(220) (2θ)	L(220) (nm)	W(311) (2θ)	L(311) (nm)
#5	0.60	0.58	14.6	0.38+1.91	25+4.6	1.14	8.0
#6	0.60	0.68	12.3	0.47+1.83	19.5+4.7	1.24	7.5
#7	0.42	0.69	12.1	0.78+2.30	11.3+3.8	1.34	6.8
#8	0	-	-	-	-	-	-

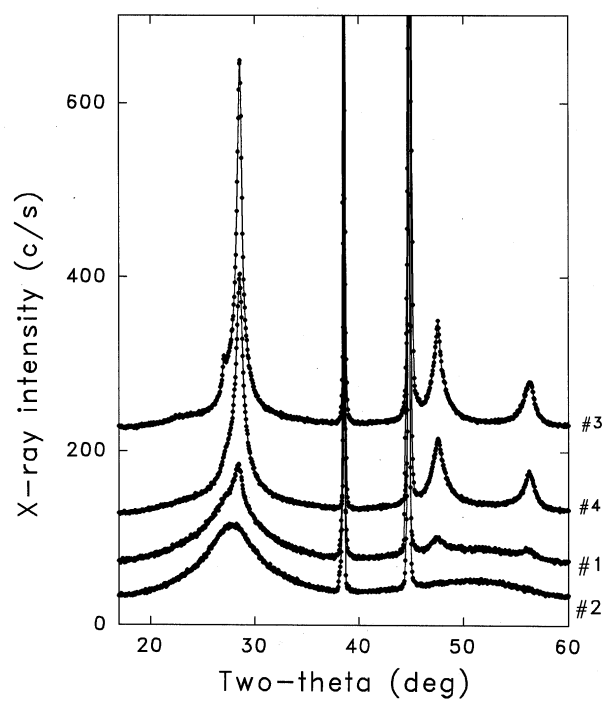


Fig. 30a. XRD patterns from first series samples on Al foil substrates.

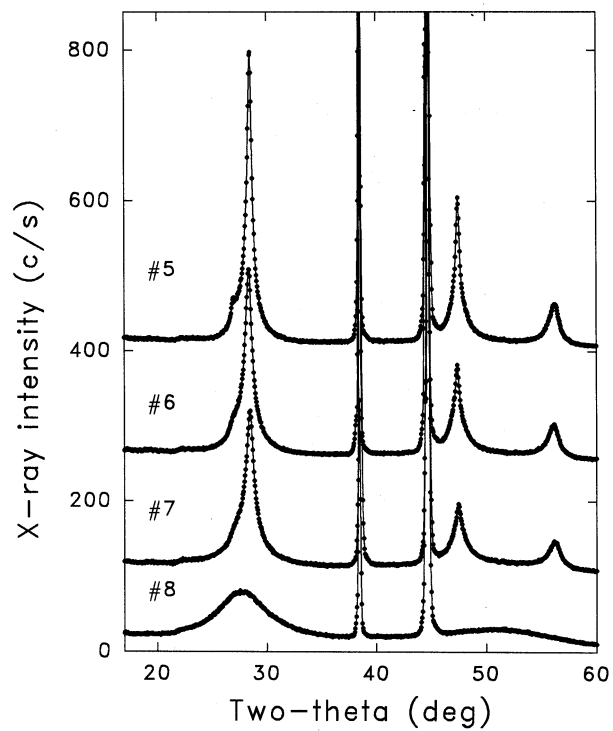


Figure 30b. XRD patterns from second series samples on Al foil substrates.

One noticeable difference for the second series was that we needed two different linewidths to fit well the (220) peak, one relatively sharp, and one relatively broad (at the same 2θ position). So two grain sizes are listed for these two components to the (220) peak. Although the fraction F is the same by XRD for samples #5 and #6, the shoulder feature near 27.1° is more obvious for #5 and the intensities are larger, probably indicating an enhanced crystallinity (also evident from larger grain sizes for #5). Also, the Raman measured at DTU suggests somewhat higher crystallinity (67%) than the XRD. In our opinion, it is just in this range ($>60\%$) that the XRD method becomes quite insensitive due to the very weak nature of the broad amorphous peak near 51° . Comparing these grain sizes with those from the first series of samples suggests generally larger grains for the second series.

Figures 31a and b show the SAXS data from all eight films. The thicknesses used are $5.0\ \mu\text{m}$ for each sample as provide by DTU. The scattering intensity is very strong and surprisingly similar for all eight samples. For comparison, the SAXS from a fully amorphous PECVD film prepared at low deposition rate ($\sim 0.1\ \text{nm/s}$) with very low void fraction ($\leq 0.01\ \text{vol.}\%$) is shown also in Fig. 31. For samples #2 and #8, which are fully amorphous according to XRD, the SAXS remains strong and comparable to the other samples with partial microcrystallinity. This suggests that the microcrystals may not contribute strongly to the SAXS. Figure 31b also shows the effect of tilting each sample at 45° relative to the beam. Any change indicates the scattering is anisotropic. The similar, significant drop in intensity shows that oriented scattering objects are present in all samples that are elongated and aligned with the growth direction. More comments on interpretation will follow the quantitative analyses and density data.

An important single quantity extracted from the SAXS data is the integrated intensity, Q , a good measure of the total inhomogeneity in each sample. These values are listed in Table 13 together with the ratio Q/Q_{45} , where Q_{45} is the value found from the 45° tilt data. The table includes the FTIR H content, $[H]$, and the samples are listed in the same order as in Table 12.

The SAXS data were fitted with a distribution of spherical objects. The shapes of all the SAXS scans are quite similar, implying a similar size distribution for all samples. Example fits and distributions are shown in Fig. 32 for one sample. The fit is not ideal at high q for the non-tilted sample since the spherical shape assumption produces a second order oscillation in this region that is not seen in the data, probably due to non-spherical shapes in reality. However, the fits are

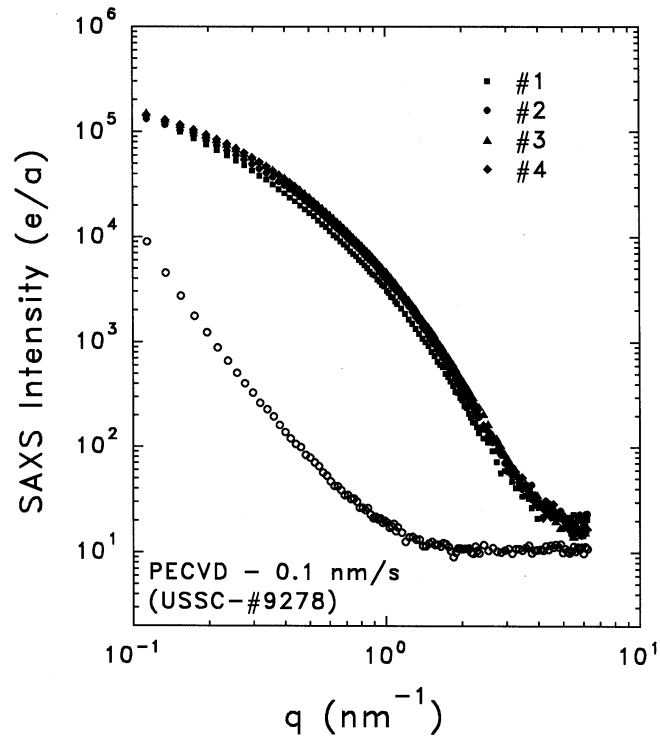


Fig. 31a. SAXS data from first series samples. Comparison data shown from PECVD a-Si:H film.

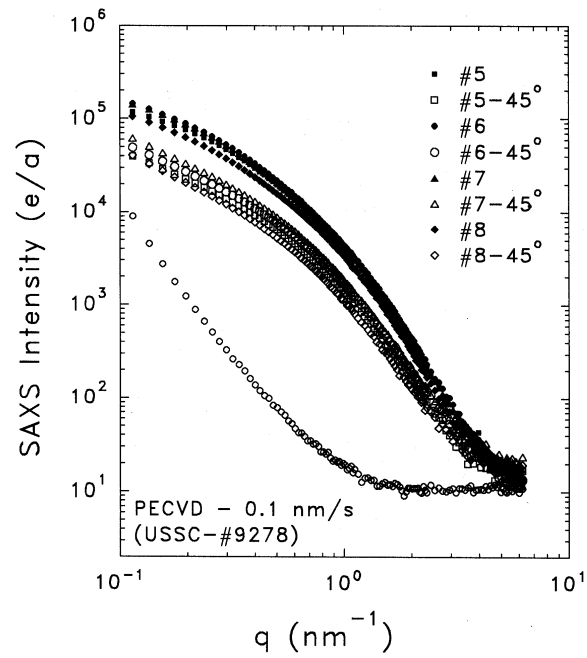


Fig. 31b. SAXS data from second series samples in both non-tilted and tilted orientations.

reasonable and should yield distributions corresponding to the approximate sizes of the scattering features. There is a well-defined lower size indicated by the flattening of the curves and an approach to a constant level at the high-q end of the data (indicated by the smallest sizes of $D = 2$ or 3 nm in the distributions). The constant level of 10-15 e/a is found for all Si:H alloys with typical H contents of 5-12 at.% H and is explained by the diffuse Laue monotonic scattering on the atomic scale. The average diameter, $\langle D \rangle$, is listed in Table 13 for the non-tilted orientation (the tilted data yield only slightly smaller $\langle D \rangle$ as shown in Fig. 32). Note in Fig. 32 that the distributions are skewed somewhat such that the most probable size is smaller than $\langle D \rangle$. These values, D_{mp} , are included in the table.

Table 13a. SAXS quantitative results and flotation densities from first series (365 mm).

Sample	[H] (at. %)	Q (10^{25} eu/cm 3)	Q/Q $_{45}$	$\langle D \rangle$ (nm)	D_{mp} (nm)	f_{max} (vol.%)	ρ_{flot} (g/cm 3)
#2	7.8	2.79	4.0	8.0	4.0	6.3	2.17
#1	8.5	2.36	4.0	8.5	4.0	5.2	2.17
#4	5.9	3.16	4.1	8.1	4.0	7.1	2.20
#3	3.1	3.31	3.5	7.6	4.0	8.4	2.19

Table 13b. SAXS quantitative results and flotation densities from second series (55 mm).

Sample	[H] (at. %)	Q (10^{25} eu/cm 3)	Q/Q $_{45}$	$\langle D \rangle$ (nm)	D_{mp} (nm)	f_{max} (vol.%)	ρ_{flot} (g/cm 3)
#5	3.7	3.08	2.8	7.7	4.0	9.3	2.23
#6	4.1	2.75	3.0	7.6	4.0	7.6	2.22
#7	4.0	2.94	2.3	8.0	4.0	10.5	2.21
#8	7.6	2.23	2.9	7.8	4.0	6.2	2.18

In order to determine the void volume fraction, f , the Q is typically used if there is no anisotropic scattering. However, due to the anisotropic scattering, a model is used based on ellipsoidal voids and the ratio Q/Q_{45} in the table. [Note that the spherical assumption used in the

fitting above would correspond to the small diameter of the ellipsoids as seen by the x-rays travelling parallel to the growth direction in the non-tilted orientation]. Basically this corrects for the strong forward scattering of the elongated objects parallel to the growth direction and gives a reasonable estimate of the void fraction *assuming all of the Q is due to voids*. The likely situation is that other features may contribute somewhat to Q (particularly in the samples with microcrystallites with their high c-Si density) so this analysis should place an *upper limit* on the void fraction. These values of f_{\max} are listed in Table 13.

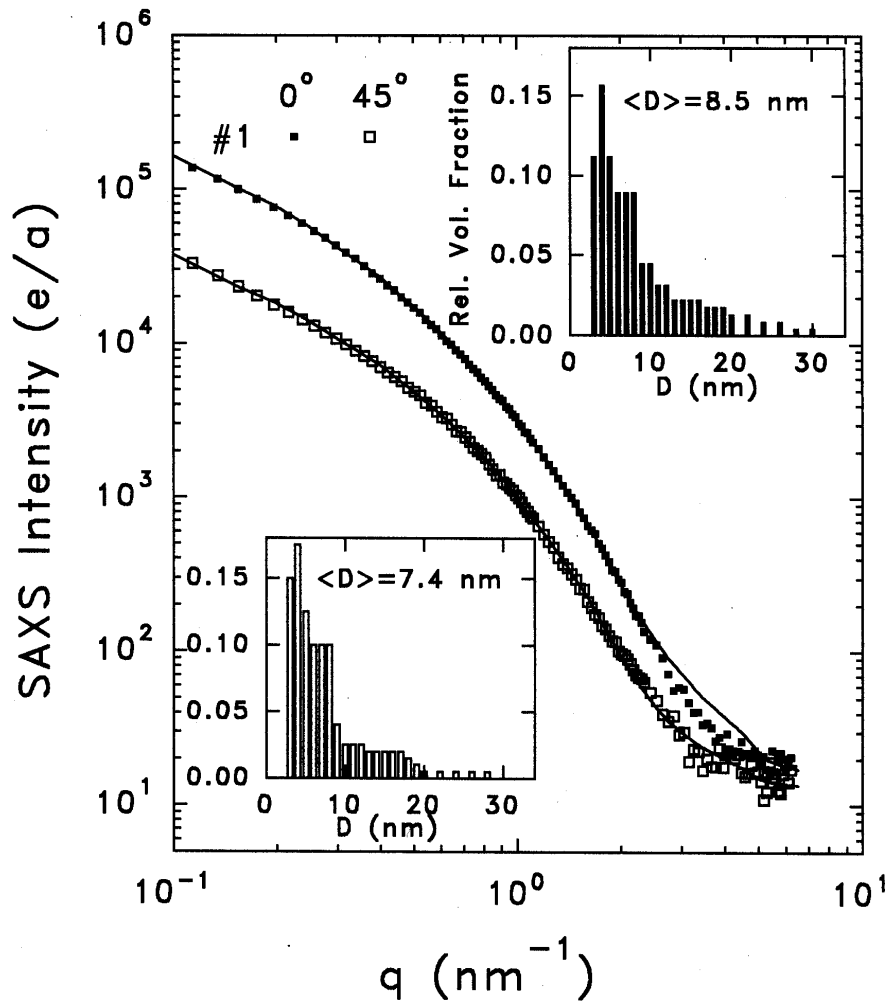


Figure 32. Examples of fits of size distributions of spheres to sample #1 data in non-tilted and 45° tilted cases. Size distributions shown in insets with average diameters indicated.

The experimental flotation density results are included in Table 13. The uncertainty in these values is $\pm 0.01 \text{ g/cm}^3$. The densities tend to be higher for the films with lower [H]. Note that the density deficits compared to c-Si ($\rho = 2.33 \text{ g/cm}^3$) are similar to or *smaller* than the calculated maximum void fractions. However, we cannot rule out the possibility that the flotation densities are too high due to the fluid actually entering some of the pores in the film (maybe it goes into the elongated pores if they emerge at the surface). One would think that a thin surface oxide might completely cover the surface and perhaps prevent the fluid from entering inside the film but this is just speculation. The evidence of Si-oxide from the XRD data of sample #3 perhaps implies internal oxidation of such elongated pores such that a significant enough fraction of the Si is oxidized in this sample to be detected by XRD.

The integrated intensities, Q , from the second series are similar or slightly smaller than those from the first series. However, the Q/Q_{45} ratios are significantly less and, based on the oriented ellipsoid model, these values lead to estimated *maximum* void fractions that are somewhat *higher* than the previous ones. This does not seem correct since the flotation densities for the second series are clearly somewhat *larger* than from the first series. This is good evidence that the SAXS must be due to other types of inhomogeneity than just voids. We have tried some calculations based on a three-phase model of dense c-Si, less-dense amorphous tissue, and microvoids but the values for Q are more than a factor of 2 too low compared to the experimental values. Even for the fully amorphous films, the void fraction is too high to be consistent with the flotation density, particularly after accounting for the reduction in density due to bonded H. One possibility is that surface roughness may be contributing significantly to the SAXS. Other possibilities are that the microstructure is more complex than just a three-phase model and/or that the ellipsoidal model used for correcting for the anisotropic effect is not very realistic.

We have typically observed strong SAXS from microcrystalline films with signals similar to those seen for the present samples. However, the large signals for the fully amorphous samples #2 and #8 are *not* typical. For lower deposition rate, fully amorphous PECVD and HWCVD a-Si:H films, the void fraction is typically near the detection limit of about 0.01 vol. % (as seen by the data for the USSC sample in Fig. 31). Even for HWCVD films grown at more than 10 nm/s, we observed a smaller SAXS signal than found here for samples #2 and #8. Thus, the ETP-CVD method used for the present samples generates a high degree of heterogeneity that is similar for *both* fully amorphous and highly microcrystalline films. The high deposition rates are apparently

generating columnar-like structures with voids likely located along the column boundaries. This has been recently confirmed by cross-sectional TEM at DTU as presented in Ref. 18. Some are highly elongated and these are sensitive to tilting, while many are more spherical and not affected by the tilting. The similar sizes of the voids and crystallites (L in Table 12 vs. $\langle D \rangle$ in Table 13) make it difficult to separate the scattering from voids and crystal.

The microstructure of the eight Delft films prepared by ETP-CVD, as determined by SAXS, are remarkably similar in spite of significant differences in the degree of crystallinity. The SAXS and flotation density are consistent with void fractions near the 5 vol. % level. The flotation densities are somewhat larger in the second series of films utilizing smaller separation of SiH_4 injection and substrate positions, implying some improvement in the compactness of the films. However, the SAXS remains unusually strong, consistent with a high degree of heterogeneity in the films studied to date. Results for solar cells made under the same two conditions used for samples #3 (first series) and #6 (second series) do show a significant improvement in efficiency (0.1% versus 1.2%, respectively) [18] but the efficiency remains quite low compared to current state-of-the-art $\mu\text{c-Si}$ based solar cells.

3.2.8 SAXS Study of UT Films Made from Disilane and Trisilane

Four a-Si:H films made by PECVD were provided by the University of Toledo (UT) for SAXS study. The goal was to investigate possible differences in microstructure of films grown near the amorphous/microcrystalline phase boundary with the two source gases disilane and trisilane. Table 14 gives some deposition conditions and V_{oc} values measured for cells with i-layers grown under nominally identical conditions.

Table 14. Preparation and V_{oc} data for UT SAXS films and solar cells.

Sample I.D.	$\text{H}_2/\text{trisilane}$	$\text{H}_2/\text{disilane}$	T_s (°C)	Power (W)	Dep. Rate (nm/s)	V_{oc} (V)
gd1027	179	-	200	3.5	0.028	1.006
gd1030	213	-	200	3.5	0.022	0.879
gd1028	-	100	200	3.5	0.025	1.004
gd1029	-	125	200	3.5	0.022	0.874

The four films were measured by XRD before folding into 8 layers for SAXS. Figure 33 shows the XRD patterns, which show that three of the films are partially microcrystalline, while one (gd1028) is fully amorphous. Sample gd1027 has a smaller microcrystalline fraction than gd1029 and gd1030. The strong lines near $2\theta = 38^\circ$ and 44° are due to the Al-foil substrate.

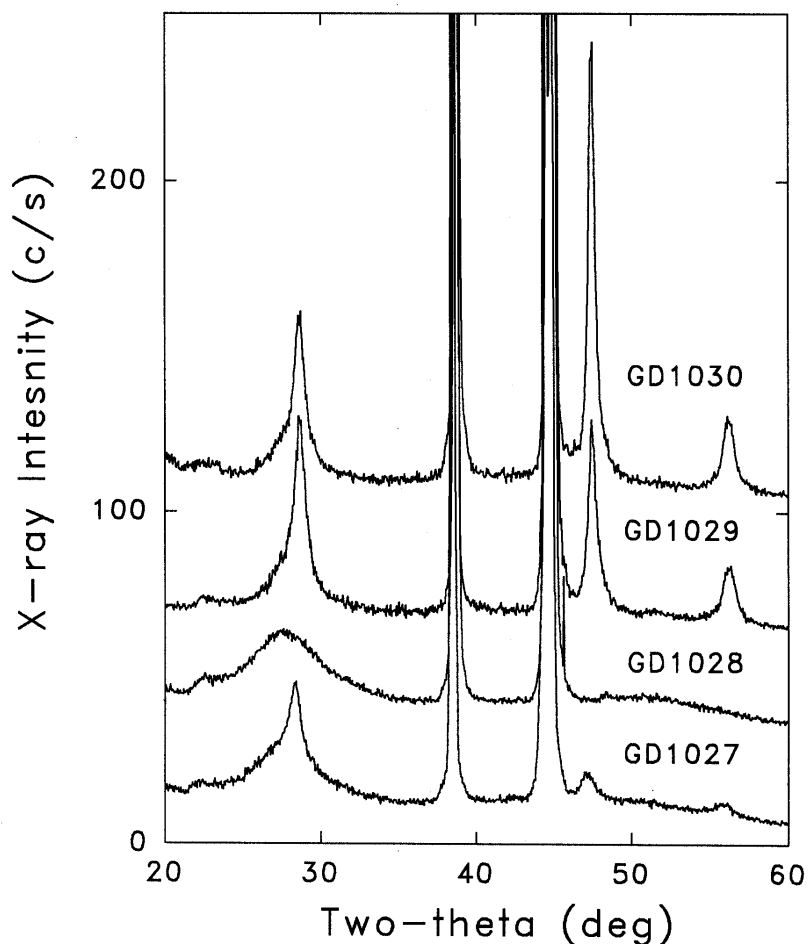


Fig. 33. XRD patterns from UT samples on Al foil substrates.

Figure 34 shows the SAXS data from all four films. The thicknesses used are $1.00 \pm 0.05 \mu\text{m}$ for each sample (provided by UT). The scattering intensity is quite strong for three samples and significantly weaker for gd1028. For comparison, the SAXS from a fully amorphous PECVD film prepared by USSC at low deposition rate ($\sim 0.1 \text{ nm/s}$) with very low void fraction ($\leq 0.01 \text{ vol.}\%$) is shown also in Fig. 34.

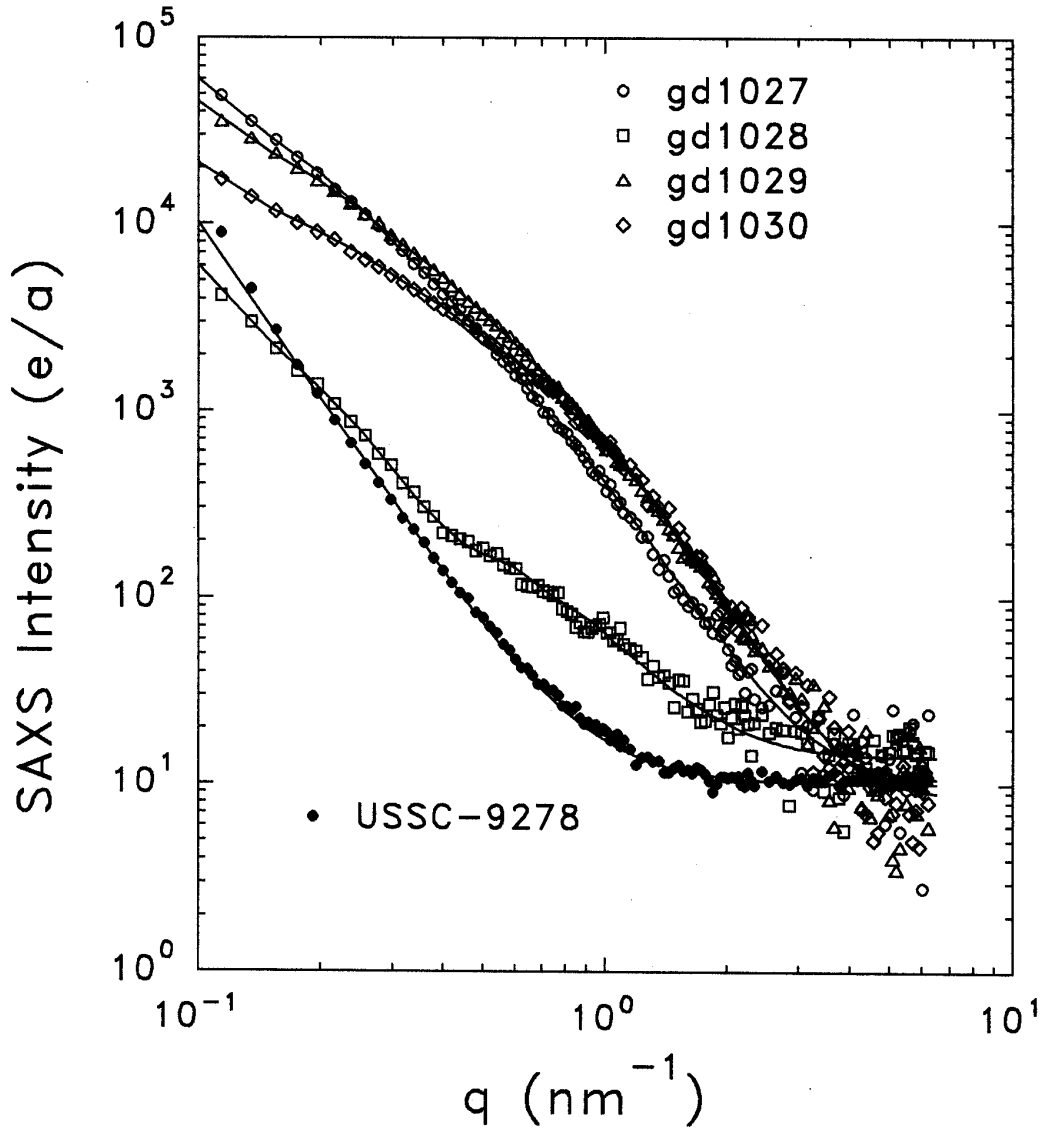


Fig. 34. SAXS data from the UT samples. Comparison data from USSC film.

The effect of tilting each sample at 45° relative to the beam was also investigated and the results indicate some preferred orientation in all four films.

An important single quantity extracted from the SAXS data is the integrated intensity, Q_N , a good measure of the total nanostructural inhomogeneity in each sample. These values are listed in Table 15 along with other fitting results: I_D = diffuse intensity (related to H content), A = Porod slope (related to surface roughness or larger-scale features), f_{\max} = maximum void fraction

assuming all of Q_N is due to voids. These values have been corrected based on the tilting ratio Q_0/Q_{45} , also included in the table. This correction is based on an assumption of ellipsoidal shapes with the long axes aligned along the growth direction.

The SAXS data were fitted as described in Ref. [8] with a distribution of spherical/ellipsoidal objects. The solid lines passing through the data in Fig. 34 are the resulting fits. The average diameter, $\langle D \rangle$, is listed in Table 15 (note: this will represent the minor axis ellipsoidal diameter in the ellipsoidal shape assumption). The distributions are skewed somewhat such that the most probable size is smaller than $\langle D \rangle$. These values, D_{mp} , are included in the table.

Table 15. SAXS quantitative results and flotation densities for UT films.

Sample	I_D (eu)	Q_N (10^{24} eu/cm ³)	Q_0/Q_{45}	A (eu/nm ³)	$\langle D \rangle$ (nm)	D_{mp} (nm)	f_{max} (vol.%)	ρ_{flot} (g/cm ³)
gd1027	10	3.46	1.9	40	10	4	1.3	2.179
gd1030	8	3.73	5.2	12	6	3	0.7	2.243
gd1028	15	0.26	3.4	5	7	3	0.06	2.177
gd1029	8	4.71	4.3	27	8	4	1.0	2.225

In addition, the experimental flotation density results are included in Table 15. They were measured with the procedure summarized in Ref. [1]. The uncertainty in these values is ± 0.01 g/cm³. The densities for gd1029 and gd1030 are significantly higher and this is consistent with the lower H content in these two films (and the smaller values of I_D). However, the values provided by UT ($C_H = 22, 18, 21, 17$ at.% for gd1027, 30, 28, 29, resp.) seem *too high* for the following reasons: (1) the expected flotation density can be estimated from $\rho(\text{g/cm}^3) = 2.291 - 0.0068C_H$ [1] (which assumes no voids) and this yields significantly lower densities than those measured (Table 15); (2) for such high C_H , I would expect higher I_D 's than those in Table 15; (3) such values seem too high compared to typical a-Si:H device quality films made under high dilution conditions (8-12 at.%). The IR results need to be checked or the IR film thicknesses need to be checked.

As shown in Ref. [1] we have typically observed strong SAXS from microcrystalline films with signals similar to those seen for the present samples. However, the V_{oc} values provided (Table 14) suggest that sample gd1027 is fully amorphous which is *not* consistent with the XRD (Fig.33) and the strong SAXS (Fig. 34). After discussions with UT, this discrepancy is attributed to a likely

thickness effect. The film used in the i-layer of the cell used for the V_{oc} measurement is significantly less than the 1.0 μm used for the SAXS film. As established earlier [19], near the onset of microcrystallinity, there is a thickness effect such that increased thickness leads to increased microcrystallinity. Thus, the gd1030 film made for SAXS has become partially microcrystalline due to thicker growth compared to the i-layer. Since this effect apparently did not occur for the pair of disilane films, this suggests that the use of trisilane may enhance the sensitivity of this thickness effect compared to disilane.

3.3 Wide-Angle X-ray Diffraction Experiments (Task 3)

Several of the above studies already utilized XRD to supplement the SAXS and TEM data and those results were included there. Here we present two studies of stand-alone XRD measurements in collaboration with the USSC group.

3.3.1 XRD Study of USSC Partially Microcrystalline Solar Cells – V_{oc} Issue

Additional x-ray diffraction experiments have been made in search of the mechanism for the light-induced increases in open circuit voltage, V_{oc} , in partially microcrystalline solar cells prepared just above the onset of microcrystallinity [20]. Our first results were presented in the NREL final report from the previous subcontract [21]. The two additional cell structures (L13774 and L13772) yielded the same *negative* result in that no changes were detected in the XRD patterns of the (220) peak before and after light soaking. These were done with care to position the sample in the same place in the XRD system and with unusually long counting times to obtain good statistics. No difference in microcrystalline fraction could be found to a precision of about 1 vol. %. Based on our earlier correlation of V_{oc} and partial microcrystallinity [17,19], changes of at least 5 vol. % could be expected for the ~ 100 mV changes in V_{oc} if this was indeed the mechanism. The microstructural changes may be occurring in nanocrystallites too small to be seen in the XRD peaks (like the (220)) and these may be less stable and susceptible to changes caused by light-soaking/annealing. Studies of the thermal stability of “on the edge” material do show less stability to crystallization [22,23]. Based on XRD, IR, and H-evolution data, nanocrystallites undetected by XRD, are postulated to exist in this material, leading to lower temperature crystallization. It was also suggested that the surfaces of the crystallites are heavily hydrogenated, implying a highly non-uniform H distribution in the “on the edge” a-Si:H [22,23]. However, our recent SANS results [3]

summarized in section 3.2.1 do not support such non-uniformity. These XRD results have been included in our recent review paper, Ref. 1.

3.3.2 XRD Study of USSC Microcrystalline Solar Cells – Deposition Effects

A set of seven samples of microcrystalline solar cells was supplied by USSC for investigation by XRD. Each sample was about 2.5 cm x 2.5 cm and contained a few dot cells on Ag/ZnO-coated stainless steel with ITO and small Au grids. Thus the XRD study is of actual i-layers of cells. Table 16 summarizes some deposition conditions and qualitative cell behavior. First, XRD scans were made of each sample, as well as a bare Ag/ZnO-coated substrate for reference, covering a full angular range from 20 to 60° 2 θ . Figure 35 shows the data from sample RF11486 and the Ag/ZnO reference on a log scale. This scale is useful for comparison since the Ag/ZnO and ITO peaks are much stronger than the μ c-Si peaks. From these data one can note the following: (1) the μ c-Si (111) and (311) peaks are clear and contain no interference from the Ag/ZnO or ITO peaks, which can readily be identified by comparing the two scans; (2) however, one of the Ag/ZnO peaks overlaps strongly with the μ c-Si (220) peak. Due to the latter, careful long-time scans were made only over the μ c-Si (111) and (311) peaks to extract more accurate results. These scans are shown in Fig. 36 where significant differences can be seen in the (111) and (311) peak regions: the linewidths vary, the intensities vary, and the size of the shoulder on the low angle side of the (111) peak seems to vary in visibility. The origin of this shoulder peak is not established, but is often seen in μ c-Si films as discussed recently in our review paper [1].

Table 16. USSC μ c-Si samples, preparation conditions, and cell behavior.

Sample ID#	Deposition Method	Thickness* (μ m)	Rate (nm/s)	Behavior
RF10973	VHF	0.86	0.3	High J_{sc} , ambient stable
RF10976	VHF	1.06	0.3	High J_{sc} , ambient unstable
RF11486	VHF	0.71	1.2	Low J_{sc} , ambient unstable
RF11538	VHF	1.13	0.3	High J_{sc} , ambient stable
RF11545	VHF	1.22	0.3	Low J_{sc}
BMW7073	MW	0.84	3.0	Low J_{sc} , ambient stable
LINE13917	RF	1.06	< 0.1	High J_{sc} , ambient stable

*Thickness estimated at USSC using optical method and includes the n and p layers.

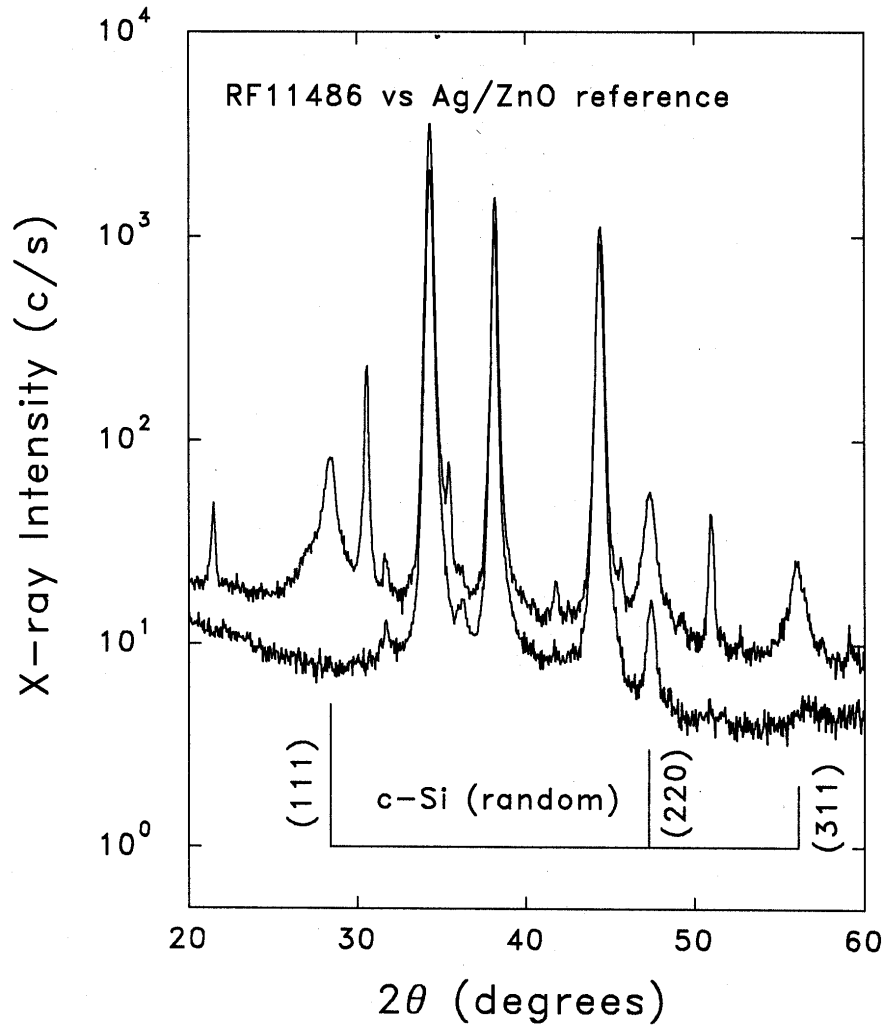


Fig. 35. XRD scans from μ c-Si cell sample RF11486 (upper pattern) compared to Ag/ZnO-coated stainless steel reference. The stick diagram identifies the peak positions and relative intensities from randomly oriented c-Si powder. Note the log scale used which enhances any weak peaks.

Each of the scans in Fig. 36 was fitted with a superposition of peaks to extract the peak position, linewidth, and integrated area of the individual peaks. Linewidths were used to estimate the grain size based on the Scherrer formula and peak positions were used to calculate the cubic lattice parameter for comparison to the known value of $a = 0.54301$ nm for bulk c-Si. Relative integrated intensities I_{220}/I_{111} and I_{311}/I_{111} were calculated for comparison to the known random powder values of 0.60 and 0.35, respectively. The values obtained for the (220) peak were based on the full scans as shown in Fig. 35 and can only be given as upper limits due to the unresolved contribution from the Ag/ZnO peak near the same position (Fig. 35). In addition, the relative integrated area of the

shoulder peak, I_s/I_{111} , was calculated. Its position occurs at $27.0 \pm 0.1^\circ$ for all samples, which is significantly lower than the a-Si:H peak position of about 27.6° , showing that it is not related to the residual amorphous phase. Information on the latter for these samples was not obtainable due to the expected weak signal and interference from the other peaks due to ITO and Ag/ZnO. In order to check whether integrated XRD signals scale with film thickness, the ratio of the integrated intensities of the (111)+(311) peaks to the provided film thickness (Table 16) is also calculated. Lower relative values of this quantity may indicate a larger amorphous fraction. Table 17 contains the results of the analyses of all the XRD data.

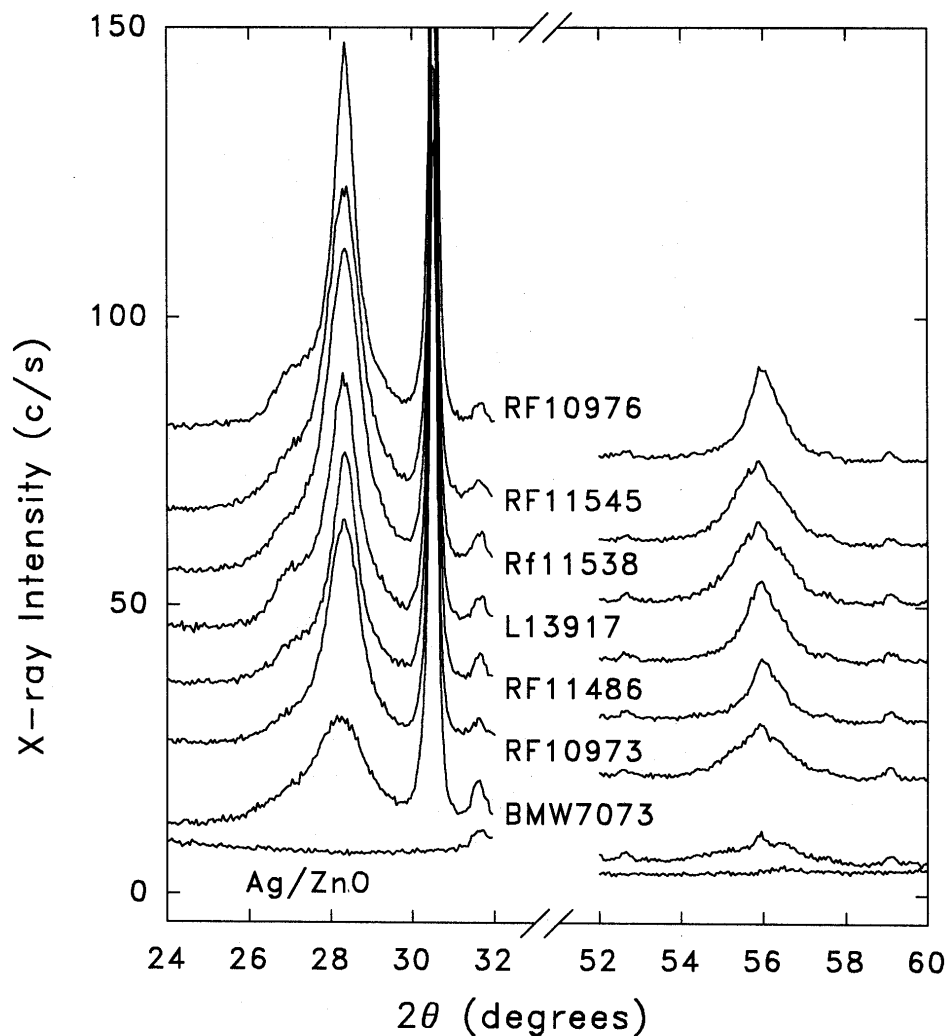


Fig.36. XRD scans over the (111) and (311) peak regions of c-Si. Each scan is shifted slightly for clarity but each one is based on the same vertical scale of x-ray counts per second. The peaks near 30.5° , 31.5° , 52.5° , and 59° are all due to ITO, although there is some contribution to the peak near 31.5° from the Ag/ZnO.

Table 17. Quantitative XRD analysis results of USSC $\mu\text{c-Si}$ solar cell i-layers. The thickness t used to calculate the number in column 2 is in μm from Table 16. L_{hkl} is the grain size estimated from the Scherrer formula for the grains with (hkl) planes parallel to the film surface. a is the cubic lattice parameter of the $\mu\text{c-Si}$ phase based on both the (111) and (311) plane spacings. Relative integrated intensities are described in the text.

Sample ID#	$I_{111}+I_{311}/t$	L_{111} (nm)	L_{311} (nm)	I_{220}/I_{111}	I_{311}/I_{111}	I_s/I_{111}	a (nm)	$\Delta a/a_{\text{c-Si}}$ (%)
RF10973	81	8.6	6.0	< 0.44	0.33	0.08	0.54445	+0.27
RF10976	103	12.5	9.6	< 0.58	0.28	0.12	0.54341	+0.07
RF11486	105	11.0	10.3	< 0.42	0.26	0.17	0.54323	+0.04
RF11538	95	8.3	6.1	< 0.42	0.28	0.09	0.54512	+0.39
RF11545	93	8.3	6.4	< 0.47	0.31	0.10	0.54560	+0.48
BMW7073	69	5.2	5.1	< 0.19	0.18	0.08	0.5456	+0.5
LINE13917	95	9.4	8.9	< 0.73	0.29	0.13	0.54362	+0.11

General comments on the results in Table 17:

- None of the samples show a preferred (220) grain orientation. In fact there is a slight (111) preference since the ratios for both the (220) and (311) orientations are close to or below the 0.60 and 0.35 random values, respectively.
- The grain sizes are all much smaller than the film thickness and the (111)-oriented grains are somewhat larger than the (311)-oriented grains.
- All the samples have $\mu\text{c-Si}$ lattice parameters that are expanded compared to c-Si. If this expansion is attributed to strain, then all the films are under compressive stress that varies from film to film. Another possibility is that the lattice parameter is a function of grain size – there is some evidence of this in that the samples with the largest grain sizes have the smallest deviations from $a_{\text{c-Si}}$.
- The data for samples RF10976 and RF11846 suggest that these two sample have the highest “degree of crystallinity”. The ratio $I_{111}+I_{311}/t$ is highest, the grain sizes are largest, the shoulder peak is larger, and the lattice expansion is least (most relaxed?). Sample LINE13917 appears to be the next in “degree of crystallinity”.
- Sample BMW7073 clearly has the least “degree of crystallinity” based on all of the above indicators.

Possible correlations of data in Table 17 with cell behavior (Table 16):

- a) Both samples with the highest “degree of crystallinity”, RF10976 and RF11486, have “ambient unstable” behavior. However, RF10976 has “high J_{sc} ” while RF11486 has “low J_{sc} ”. Note that RF10976 has a somewhat larger I_{220}/I_{111} and slightly larger (111) grains, perhaps promoting higher J_{sc} .
- b) Note that RF10973 and RF11538 both have “high J_{sc} , ambient stable” behavior and have quite similar XRD parameters. On the other hand, sample RF11545 has similar parameters to these, yet yields “low J_{sc} ”. The latter sample does have the highest lattice expansion (most compressive stress?) of the set.
- c) Sample BMW7073 has the smallest grain sizes and least “degree of crystallinity”, likely correlating with the “low J_{sc} ”.
- d) Sample LINE13917 seems to stand out with the largest I_{220}/I_{111} ratio, but it has intermediate grain sizes, intermediate lattice expansion, and a relatively large I_s/I_{111} , so a correlation with the “high J_{sc} , ambient stable” behavior is not clear.

4. ACKNOWLEDGEMENTS

This research was enabled by the supply of high-quality, specialized samples prepared by groups at NREL, USSC, MVSsystems, IEC, BP-Solar, University of Toledo, Delft Technical University, and KAIST.

5. REFERENCES

- [1] D. L. Williamson, Solar Energy Materials & Solar Cells 78, 41 (2003).
- [2] E. Sutter and D. L. Williamson, Appl. Phys. Lett., submitted.
- [3] D. L. Williamson, D. W. M. Marr, J. Yang, B. Yan, and S. Guha, Phys. Rev. B 67, 075314 (2003).
- [4] S. Guha, Y. Yang, A. Banerjee, B. Yan, and K. Lord, Solar Energy Materials & Solar Cells 78, 329 (2003).
- [5] A.H. Mahan, Y. Xu, D.L. Williamson, W. Beyer, J.D. Perkins, M. Vanecek, L.M. Gedvilas, and B.P. Nelson, J. Appl. Phys. 90 (2001) 5038.

- [6] D.L. Williamson, D.W.M. Marr, E. Iwaniczko, and B.P. Nelson, *Thin Solid Films* 430, 192 (2003)
- [7] S. Sugiyama, J. Yang, and S. Guha, *Appl. Phys. Lett.* 70, 378 (1997)
- [8] D.L. Williamson, *Mater. Res. Soc. Symp. Proc.* 377 (1995) 251.
- [9] O. Ebil, R. Aparicio, S. Hazra, R. Birkmire, and E. Sutter, *Thin Solid Films* 430, 120 (2003).
- [10] G. Ganguly, in *Record of the 16th NREL Amorphous and Thin-Film Silicon Review Meeting*, January 9 & 10, 2003.
- [11] B.P. Nelson, Y. Xu, D.L. Williamson, D. Han, R. Braunstein, M. Boshta, and B. Alavi, *Thin Solid Films* 430, 104 (2003).
- [12] B.P. Nelson, Y. Xu, D.L. Williamson, B. von Roedern, A. Mason, S. Heck, A.H. Mahan, S.E. Schmitt, A.C. Gallagher, J. Webb, and R. Reedy, *Mat. Res. Soc. Symp. Proc.* 507, 447 (1998).
- [13] D.L. Williamson, Y. Xu, B.P. Nelson, in *NCPV Photovoltaics Program Review*, AIP Conf. Proc. No. 462, Ed. by M. Al-Jassim, J.P. Thornton, J.M. Gee (AIP, Woodbury, NY 1999) p. 272.
- [14] Y. Xu, B.P. Nelson, D.L. Williamson, L.M. Gedvilas, and R.C. Reedy, *Mat. Res. Soc. Symp. Proc.* 762, A10.2 (2003).
- [15] J.Y. Ahn, K.H. Jun, M. Konagai, and K.S. Lim, *Conference Record IEEE Photovoltaic Specialists Conf.*, vol. 29, 1039 (2002).
- [16] E.A.G. Hamers, A.H.M. Smets, C. Smit, J.P.M. Hoefnagels, W.M.M. Kessels, and M.C.M. van de Sanden, *Mat. Res. Soc. Symp. Proc.* 664, A4.2 (2001).
- [17] D.L. Williamson, *Mat. Res. Soc. Symp. Proc.* 557, 251 (1999).
- [18] C. Smit, D.L. Williamson, M.C.M. van de Sanden, and R.A.C.M.M. van Swaaij, *Mat. Res. Soc. Symp. Proc.* 762, A15.3 (2003).
- [19] S. Guha, J. Yang, D.L. Williamson, Y. Lubianiker, J.D. Cohen, and A.H. Mahan, *Appl. Phys. Lett.* 74, 1860 (1999).
- [20] K. Lord, B. Yan, J. Yang, and S. Guha, *Appl. Phys. Lett.* 79, 3800 (2001).
- [21] D.L. Williamson, *Final Technical Progress Report*, 22 May 1998 – 15 October 2001, NREL/SR-520-31908 (2002).

- [22] A.H. Mahan, W. Beyer, D.L. Williamson, J. Yang, and S. Guha, *Phil. Mag. Lett.* 80, 647 (2000).
- [23] A.H. Mahan, Y. Yang, S. Guha, and D.L. Williamson, *Phys. Rev. B* 61, 1677 (2000).

REPORT DOCUMENTATION PAGE			<i>Form Approved</i> OMB NO. 0704-0188	
Public reporting burden for this collection of information is estimated to average 1 hour per response, including the time for reviewing instructions, searching existing data sources, gathering and maintaining the data needed, and completing and reviewing the collection of information. Send comments regarding this burden estimate or any other aspect of this collection of information, including suggestions for reducing this burden, to Washington Headquarters Services, Directorate for Information Operations and Reports, 1215 Jefferson Davis Highway, Suite 1204, Arlington, VA 22202-4302, and to the Office of Management and Budget, Paperwork Reduction Project (0704-0188), Washington, DC 20503.				
1. AGENCY USE ONLY (Leave blank)	2. REPORT DATE January 2004	3. REPORT TYPE AND DATES COVERED Annual Technical Progress Report 1 April 2002–31 August 2003		
4. TITLE AND SUBTITLE Structure of Silicon-Based Thin Film Solar Cell Materials: Annual Technical Progress Report, 1 April 2002–31 August 2003		5. FUNDING NUMBERS PVP45001 XDJ-2-30630-27		
6. AUTHOR(S) D.L. Williamson				
7. PERFORMING ORGANIZATION NAME(S) AND ADDRESS(ES) Department of Physics Colorado School of Mines Golden, Colorado 80401		8. PERFORMING ORGANIZATION REPORT NUMBER		
9. SPONSORING/MONITORING AGENCY NAME(S) AND ADDRESS(ES) National Renewable Energy Laboratory 1617 Cole Blvd. Golden, CO 80401-3393		10. SPONSORING/MONITORING AGENCY REPORT NUMBER NREL/SR-520-35227		
11. SUPPLEMENTARY NOTES NREL Technical Monitor: B. von Roedern				
12a. DISTRIBUTION/AVAILABILITY STATEMENT National Technical Information Service U.S. Department of Commerce 5285 Port Royal Road Springfield, VA 22161			12b. DISTRIBUTION CODE	
13. ABSTRACT (<i>Maximum 200 words</i>): The purpose of this research is to achieve a better understanding to improve materials used as the intrinsic layers of amorphous and microcrystalline silicon-based solar cells. Fundamental structural properties will be investigated on atomic and nano-scales. A powerful combination of techniques will be used: analytical high-resolution transmission electron microscopy (HRTEM), including special associated spectroscopic methods, small-angle scattering techniques (SAXS, ASAXS, SANS), and conventional wide-angle X-ray diffraction (XRD).				
14. SUBJECT TERMS: PV; intrinsic layers; amorphous silicon; microcrystalline; solar cells; atomic and nano-scales; high-resolution transmission electron microscopy (HRTEM); small-angle scattering techniques (SAXS); X-ray diffraction (XRD).			15. NUMBER OF PAGES	
			16. PRICE CODE	
17. SECURITY CLASSIFICATION OF REPORT Unclassified	18. SECURITY CLASSIFICATION OF THIS PAGE Unclassified	19. SECURITY CLASSIFICATION OF ABSTRACT Unclassified	20. LIMITATION OF ABSTRACT UL	